



HAL
open science

Inverse identification of pipeline steel mechanical state by means of coupled magnetic measurements and artificial neural networks

Z. Maazaz, Olivier Hubert, E. Zemmouri

► **To cite this version:**

Z. Maazaz, Olivier Hubert, E. Zemmouri. Inverse identification of pipeline steel mechanical state by means of coupled magnetic measurements and artificial neural networks. *NDT & E International*, 2022, pp.102782. 10.1016/j.ndteint.2022.102782 . hal-03915956

HAL Id: hal-03915956

<https://hal.science/hal-03915956>

Submitted on 30 Dec 2022

HAL is a multi-disciplinary open access archive for the deposit and dissemination of scientific research documents, whether they are published or not. The documents may come from teaching and research institutions in France or abroad, or from public or private research centers.

L'archive ouverte pluridisciplinaire **HAL**, est destinée au dépôt et à la diffusion de documents scientifiques de niveau recherche, publiés ou non, émanant des établissements d'enseignement et de recherche français ou étrangers, des laboratoires publics ou privés.

Inverse identification of pipeline steel mechanical state by means of coupled magnetic measurements and artificial neural networks

Z. Maazaz^{a,b,*}, O. Hubert^a, E. Zemmouri^b

^a *Université Paris-Saclay, CentraleSupélec, ENS Paris-Saclay, CNRS, Laboratoire de Mécanique Paris-Saclay, Gif-sur-Yvette, France.*

^b *Moulay Ismail University, ENSAM Meknes, LM2I Laboratory, Meknes, Morocco.*

Abstract

Artificial neural networks are widely used to develop models able to predict properties of interest by learning and establishing relationships between inputs and outputs of a system. It is particularly relevant for the inversion process in the framework of Non-Destructive Testing (NDT) involving strongly non-linear and non-monotonic behavior and/or saturations. The case-study considered in this work is a magnetic material subjected to uniaxial mechanical stress, plastic strain and magnetic field. An Artificial Neural Networks (ANN) model is proposed to predict the corresponding remanent magnetization, coercive field and the maximum magnetization as target properties. A series of experimental data made of various magneto-mechanical measurements are used to train, evaluate and validate the ANN model. The proposed model suitably predicts the magnetic properties of a second specimen of the material in the same magnetic field, plastic strain and stress ranges as the first specimen. An inverse ANN is then proposed to evaluate the mechanical loading and the plastic strain from the magnetic signature. Unique and accurate solutions are found that proves the relevance of machine learning approach in such NDT application.

1. Introduction

The non-destructive testing process of materials and structures usually involves the evaluation of a target state through the measurement of another physical quantity. For example, magnetic behavior is known to be sensitive to any mechanical loading depending on the loading level (elastic, plastic), the loading sign (tension, compression) and loading multiaxiality and heterogeneity (first or second order residual stress) [1, 2, 3, 4, 5, 6]. The correlation between mechanical, metallurgical and magnetic states has received increasing attention

*Corresponding author

Email address: zakariae.maazaz@ens-paris-saclay.fr (Z. Maazaz)

these last years because improving the performance of materials and structures (mechanical thresholds, fatigue lifetime, etc.) requires a better knowledge of their mechanical state (residual stress, microstructure after thermomechanical treatment)[7, 8, 9]. Besides well-known techniques like variation of electromagnetic circuit impedance (Eddy current set-up) or flux lines modification, some new non-destructive testing (NDT) or monitoring (NDM) techniques have been developed to measure magnetic indicators of the mechanical state. In particular, indicators of hysteresis magnetic cycle like the coercive field or the remanent magnetization are interesting quantities. The measurement of other indicators like hysteresis losses, incremental permeability obtained at variable frequencies or even magnetostriction can be used as well for NDT process.

The coercive field is for example easily evaluated by the Barkhausen noise method. In [10] the magnetic Barkhausen noise method is employed for evaluating the change of microstructure induced by creep/aging of high chromium steel subjected to different creep test conditions as stress and temperature. Some other more recent NDT methods have been developed to detect very small variations in the magnetic field surrounding a massive ferromagnetic structure, such as a tank [11] or pipe [12]. In particular, the detection of damage in buried pipelines becomes possible [13]. The local plastic deformation and the creation of long range residual stresses lead to a significant change of remanent magnetization of the material that can be detected by fluxgate sensors.

However, reverse identification requires models allowing for the association of magnetic quantities to mechanical state. This process remains an open problem since it faces major difficulties. The most classic way consists in getting a fully coupled magneto-elastic or magneto-plastic modeling defined at the appropriate scale and in setting up an inverse identification procedure. The most advanced magneto-elastic coupling models (i.e. taking into account the multi-axial stress state or the Villari reversal) derive their precision from an accurate description of the microstructure including appropriate scale transitions [14]. However, these models are too slow and lead to more qualitative than quantitative estimations to allow for an efficient identification process. Some simplified approaches have been therefore proposed in the recent years. The most successful macroscopic model, since it is based on a rigorous magneto-elastic approach, are the so-called Simplified Multiscale Modeling (SMM) and multidomain modeling (MMD) [15, 16]. Even if the physical content of these models is strong, gaps between model and experiments remain significant, making any inverse identification process fail. Mostly anhysteretic, they rarely, or unconvincingly, include a satisfactory description of the evolution of hysteresis under stress. Models including plasticity are even rarer. Most of them are plastic strain (scalar description) parameters dependent models (e.g. Jiles-Atherton-Sablik model [17]). A more recent macroscopic approach for the modeling of the influence of plastic deformation on the magnetic behavior of ferromagnetic materials have been proposed by [18]. The main assumption is that the material must be considered as a two-phase material, with a mechanically hard phase and a mechanically soft phase. This model brings advantage of considering not only a plastic state but also of being able to deal with a superposition between plastic

state and multiaxial stress state, a situation often met in deformed structures. As for models of the same family, description of hysteresis remains a weak point.

As the prediction of the magnetic hysteresis depending on the mechanical state is complex, the inverse procedure is still out of reach. The problem lends itself to being solved using Artificial Neural Networks (ANN), which decouples the physics from the problem and relates a set of input parameters directly to a set of output parameters. Interest in artificial intelligence (AI) to model the behavior of material (*i.e.* a physical response to a physical loading) has grown in the recent years. ANN is one of the most known algorithms used for AI. ANN uses an architecture of basic mathematical functions that try to simulate a brain neuron mechanism. Such approaches attempted to mimic relationships between inputs and outputs (experimental data) using computing systems with learning capabilities. ANN knows various applications in materials science in general and particularly for magnetic materials. It is especially interesting for the modeling of complex problems involving non linear relationships between inputs and outputs. For example, [19] used ANN to predict the magnetostriction characteristics of transformer core material and showed good ability to fit experiments. Similarly, a Genetic Algorithm (GA) based Back-Propagation (BP) neural network was used to characterize the crack depth and width in a ferromagnetic material in [20]. In [21] a computational model for dynamic hysteresis in laminated SiFe alloys was proposed. In [22] an ANN inverse model has been developed to predict microstructure for desired material properties in Galfenol.

In this paper a new approach for the modeling of the influence of plastic deformation on the magnetic behavior of ferromagnetic materials based on AI is proposed. This approach uses ANN as a method for predicting magnetic behavior including nonlinear and non-monotonous phenomena. Parameters addressed are the remanent magnetization M_r , the coercive field H_c and the maximal magnetization M_{max} . They evolve as function of the maximal magnetic field H_{max} , uniaxial stress σ and plastic strain level ϵ_p carried out by tensile strengthening. The first part of the paper presents the results of an experimental study where the variation of magnetic behavior with stress and plastic strain is addressed. ANN modeling is then presented in the second part. The third part presents the inverse model allowing for the prediction of the mechanical state (applied stress and plastic deformation level) from magnetic data (namely maximal magnetic field strength, maximal magnetization, coercive field and remanent magnetization). Performances of the procedure are evaluated.

2. Influence of stress and plastic strain on magnetic behavior of a pipeline steel

2.1. Experimental procedure and material

A pipeline steel (wt%C=0.19, wt%Mn=0.85, wt%Si=0.2, Fe: bal.) has been used for this study. Its microstructure consists in about 40%vol. pearlite islands

dispersed in a α -iron matrix. Combination of phases leads to a soft ferromagnetic material [12]. Specimens are taken from a 150mm diameter pipeline. They consist of 180 mm long, 12 mm wide, and 4 mm thick strips. A MTS uniaxial electro-hydraulic machine (displacement controlled) has been used to apply plastic strain and to control stress at different loading levels. The experimental magnetic device enables magnetic measurements on plastically strained samples with or without applied stress using quasi-static triangular magnetic field conditions. Set-up is composed of a primary coil to magnetize the sample and a pick-up coil (B-coil) to measure the electromotive force. The magnetic field is estimated by applying Ampere’s law to the magnetic circuit. Two high permeability ferrite yokes have been assembled with the sample to close the magnetic circuit and reduce the macroscopic demagnetizing field, making the magnetic field linearly dependent on electrical current. The bench used is illustrated in figure 1, a 3D illustration of the bench is given in figure ???. Measurements have been first performed on unstrained samples providing reference magnetic behavior. Measurements have been next performed on samples submitted to an increasing plastic deformation level and under increasing tensile stress. Measurements have been conducted using two specimens referenced as A and B specimens, machined in the same pipeline tube. Experimental results carried out with specimen A are presented and discussed in the core of manuscript. A large part of these results are used for the ANN training. Experimental results carried out with specimen B are gathered in Appendix A. They are used for the ANN validation step.

2.2. Experimental results

Figure 3 illustrates the reference first magnetization curve and hysteresis loop of the material. The loop can be characterized by three magnetic parameters: the remanent magnetization M_r defined as the magnetization that remains in a ferromagnetic material after the removal of applied magnetic field, the coercive field H_c which indicates the external magnetic field required to demagnetize a material (also seen as the magnetic field that must be overcome to initiate irreversible displacement of magnetic domain walls in a material); finally, the maximum magnetization M_{max} that is the magnetization reached at the maximum magnetic field strength H_{max} . We will focus in particular on the evolution of these parameters according to the applied stresses and the plastic strain level.

Figure 4 illustrates the stress-strain curve of the material obtained by applying a mechanical loading-unloading at increasing plastic strain levels. The yield stress is close to 300MPa (where a first non-linearity can be detected). It is immediately followed by a stress plateau underlining a first strengthening process within the material (usually inhomogeneous). A classical hyperbolic homogeneous strengthening is next observed until stress saturation (not plotted) for a maximal deformation level reaching 20%.

Figures 5a-d gather different magnetic characteristics obtained with specimen A. Figure 5a illustrates the first magnetization curves obtained at different

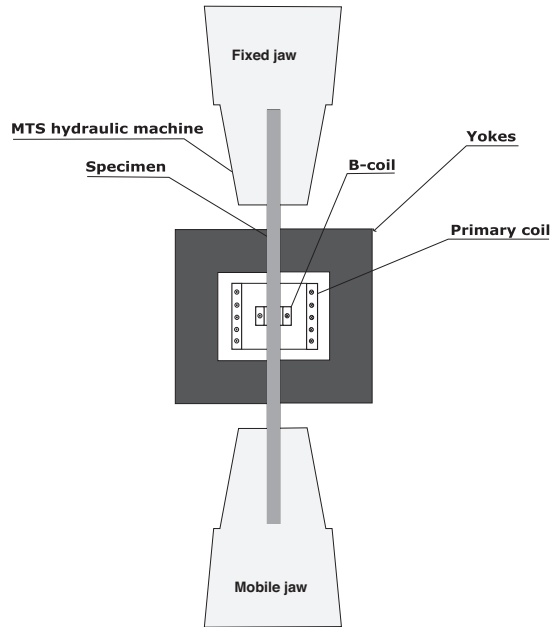


Figure 1: Set-up used to measure the magneto-mechanical behavior.

stress levels remaining in the elastic domain of the material ($\epsilon_p = 0$). Results are in agreement with what is expected for a standard steel [1]: a uniaxial tension leads to an increase of the permeability of the material for a wide magnetic field range. This increasing gradually saturates at higher stress (curve $M(H)$ at 200 MPa lies under curve $M(H)$ at 120 MPa). This non-monotony has recently been interpreted as a stress second-order phenomenon (morphic effect) [23]. At a higher magnetic field, curves meet and can even cross. This crossing point is known as the Villari reversal [2] (observation would have been easier for a higher magnetic field strength range). This phenomenon is directly related to the rotation of the magnetic moments at high field [1]. The effect of the magnetostrictive constant $\lambda_{111} < 0$ becomes dominant in the magnetoelastic component of the material free energy [24]. Magnetic hysteresis cycles presented in figure 5b undergo the same effect. Two cycle crossing zones are also highlighted for magnetic field levels close to the coercive field. Readers can refer to the works of [25] for more information about this singular point. We observe on these cycles a strong variation of the coercive field and of the remanent magnetization.

Figure 5c shows the evolution of the first magnetization curve of the material with plastic deformation at zero applied stress. Plastic deformation leads to a strong reduction of magnetic permeability from the first percentages of deformation, concurring with conclusions of many other authors [1, 2, 3, 5]. This effect is also highly non-linear: the variation in magnetization between 0% and 5% is for example much greater than between 10% and 15%. Curves meet gradually



Figure 2: 3D presentation of the magneto-mechanical system

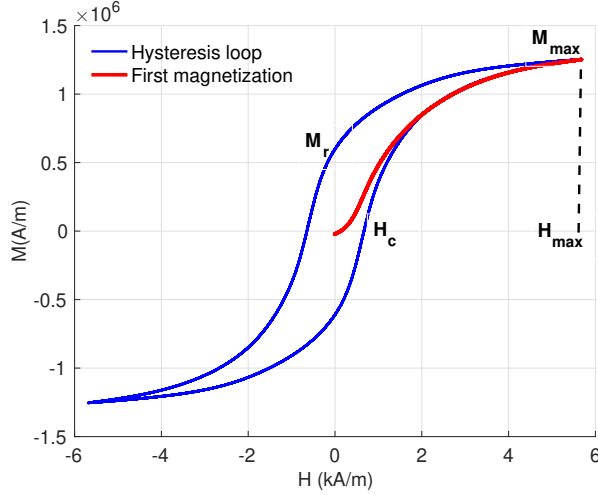


Figure 3: Initial magnetization curve (red), hysteresis loop (blue) and magnetic parameters (black).

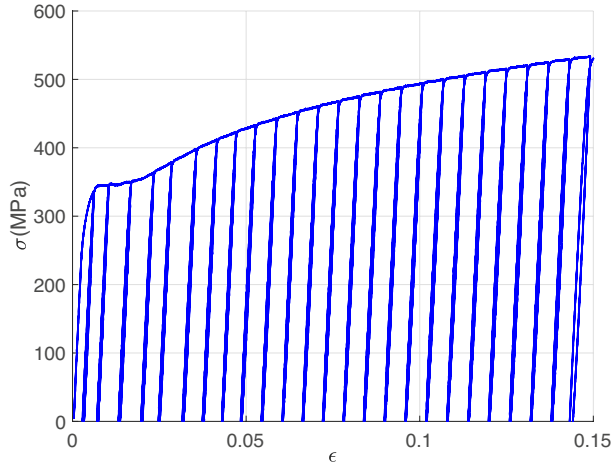


Figure 4: Quasistatic stress-strain curve of pipeline steel exhibiting the different unloadings at different plastic strain levels ($\dot{\epsilon} = 1.0 \times 10^{-4} \text{s}^{-1}$).

at higher magnetic field. However, no crossing is observed in the magnetic field range of experiments. The associated hysteresis cycles are presented in figure 5d showing the same evolution. Coercive field and remanent magnetization present variations close to those observed under compressive stress and consistent with literature [4]. The two crossing zones are a consequence of the opposite variations of coercive field and remanent magnetization with plastic strain. Two major theories are proposed to explain the effect of plasticity on magnetic

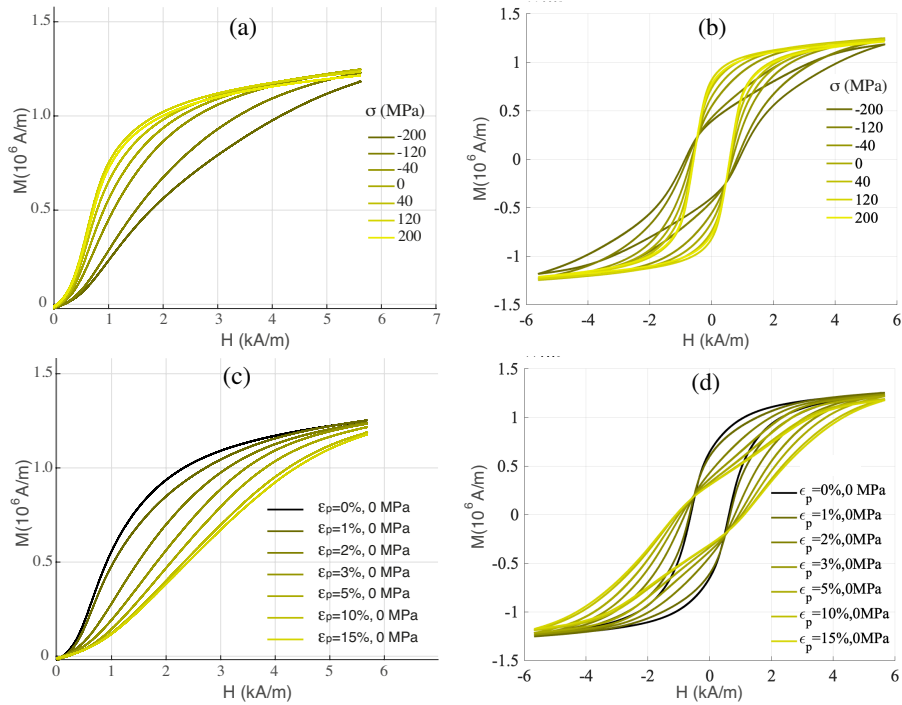


Figure 5: (a) First magnetization curves for different applied stress levels (elastic domain); (b) hysteresis loops for different applied stress levels (elastic domain); (c) first magnetization curves for different plastic strain levels at the unloaded state; (d) hysteresis loops for different plastic strain levels at the unloaded state.

behavior. Some authors incriminate the defects density (dislocations, dislocation clusters and tangles) which increases drastically with plasticity and its effects on the mobility of the magnetic microstructure (magnetic walls, magnetic domains) under magnetic field [26, 27]. Other authors have observed that plasticity is generally accompanied by a displacement of the elastic domain in the stress space: after tensile testing, most of metallic materials exhibits an asymmetry of new yield stresses in tension and in compression. This phenomenon is called the Baushinger effect [28] or kinematic hardening (*backstress* term is sometimes employed). It reflects the existence of internal stress fields in the material. Hug and Hubert [29, 3] were thus the first to show that magnetic parameters such as the initial permeability or the coercive field evolve linearly with the kinematic hardening whereas it presents a strongly nonlinear evolution with the plastic deformation or dislocations density. The effect of plasticity would thus be similar to a local magneto-elastic effect, which explains the proximity of the effects observed with those due to a macroscopic applied stress remaining in the elastic domain.

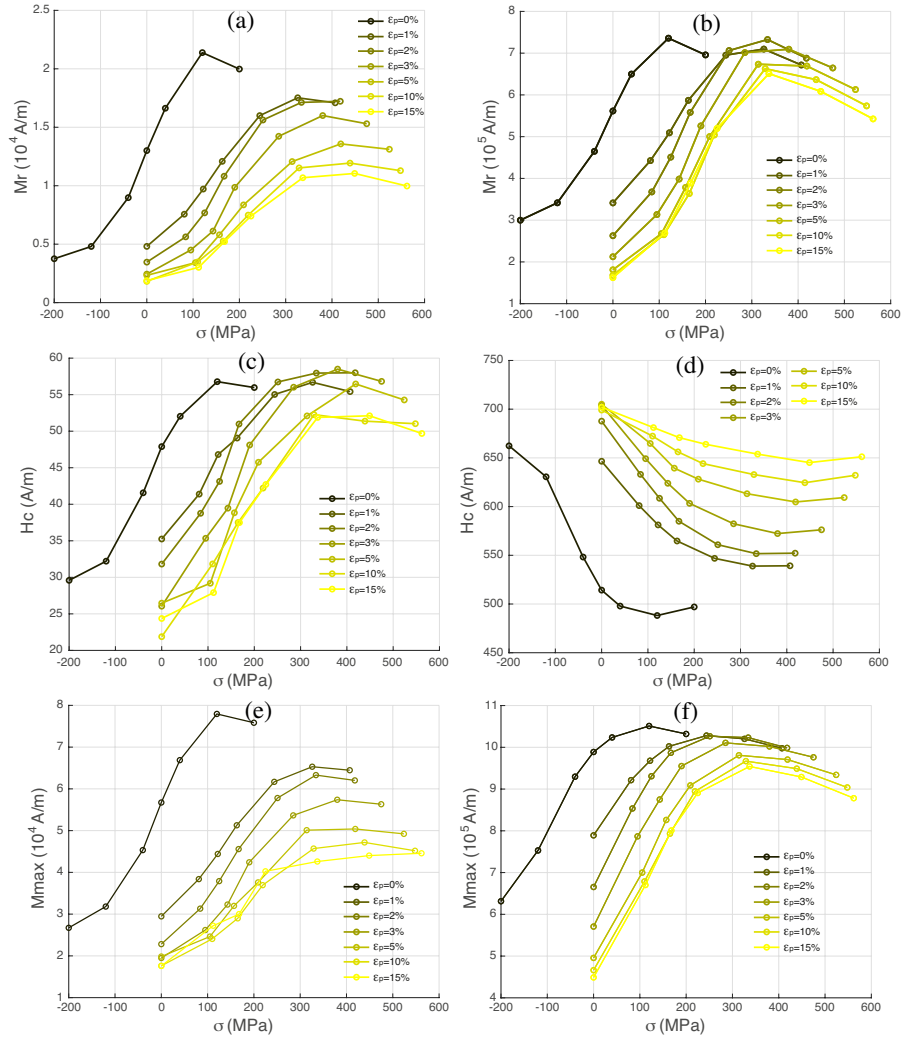


Figure 6: Magnetic indicators for specimen A - Remanent magnetization according to mechanical stress (a) $H_{max} = 230 A/m$, (b) $H_{max} = 2250 A/m$; coercive field according to mechanical stress (c) $H_{max} = 230 A/m$, (d) $H_{max} = 2250 A/m$; maximum magnetization according to mechanical stress (e) $H_{max} = 230 A/m$, (f) $H_{max} = 2250 A/m$.

We restrict now our study and comments to some specific points, acting like a NDT controller who can access to a reduced number of key material parameters, namely, the remanent magnetization, the coercive field and the maximum magnetization in relation with the tensile stress and the plastic strain.

The following illustrations concern results obtained for at low and high maximum magnetic field levels: $H_{max} = 230 A/m$ and $H_{max} = 2250 A/m$.

Results reported in Figure 6a and 6b show that the remanent magneti-

zation increases according to stress until a threshold (that increases with increasing plastic strain level) where a remanent magnetization decreasing begins. This non-monotony is symptomatic of Villari reversal [30]. Even if amplitudes reached and threshold values do change, variations observed for both maximal magnetic field strengths are close to each other. A same comment can be brought for variations of maximal magnetization plotted in figures 6e and 6f: increasing of M_{max} with stress whatever the plastic strain level until a plastic strain dependent stress threshold where M_{max} begins to decrease.

Figures 6c and 6d shows that coercive field variations with stress strongly depend on the maximum magnetic field. For cycles obtained at low maximal magnetic field ($H_{max}=230\text{A/m}$, figure 6c), coercive field increases with plastic strain level but decreases according to applied stress. For cycles obtained at high maximal magnetic field ($H_{max}=2250\text{A/m}$, figure 6d), coercive field still increases with plastic strain level but it increases now according to applied stress. As for remanent and maximal magnetization, a non-monotony occurs after a stress threshold. The variation of coercive field with increasing plasticity is consistent with results of literature. But there are few available results in literature that show the effect of an applied stress on coercive field at different maximal magnetic field levels. Coercive field is generally measured from a major cycle obtained using a high magnetic field amplitude and its decreasing with stress (figure 6d) is a known result [25]. The change in monotony which takes place at a lower maximum magnetic field (between 230A/m and 2250A/m) has to be considered in regards with a generally lower level of magnetization which is itself stress sensitive. These results show how difficult it can be to identify a mechanical state from magnetic information, especially when information is partial. Indeed results easily show that several mechanical states (σ, ϵ_p) can correspond to a same remanent or maximum magnetization. The sensitivity of coercive field to mechanical state that depends strongly on the maximum magnetic field level is another strong issue. As indicated in introduction, apart from a few very targeted attempts (based for example on the observation of a displacement of the remanent magnetization characteristics under stress during plasticity: see figure 6b and [12]), most phenomenological or physically based models fail to allow for an inverse identification. We propose in the next sections of the paper an inverse identification approach using neural networks. The direct process consists in being able to predict the output quantities (M_r, H_c and M_{max}) according to the mechanical input parameters (σ, ϵ_p) complemented by the knowledge of the maximum field level H_{max} .

3. Artificial neural network modeling

Artificial Neural Network is a computational model able to extract (*learn*) complex, nonlinear relationships between variables from a representative dataset that describes a given physical phenomenon. This learning method mimics a biological nerve system by the use of several numbers of *neurons* (*elementar input/output logical schemes*) interconnected to each other [31]. This computational/mathematical technique is especially useful for simulations of any cor-

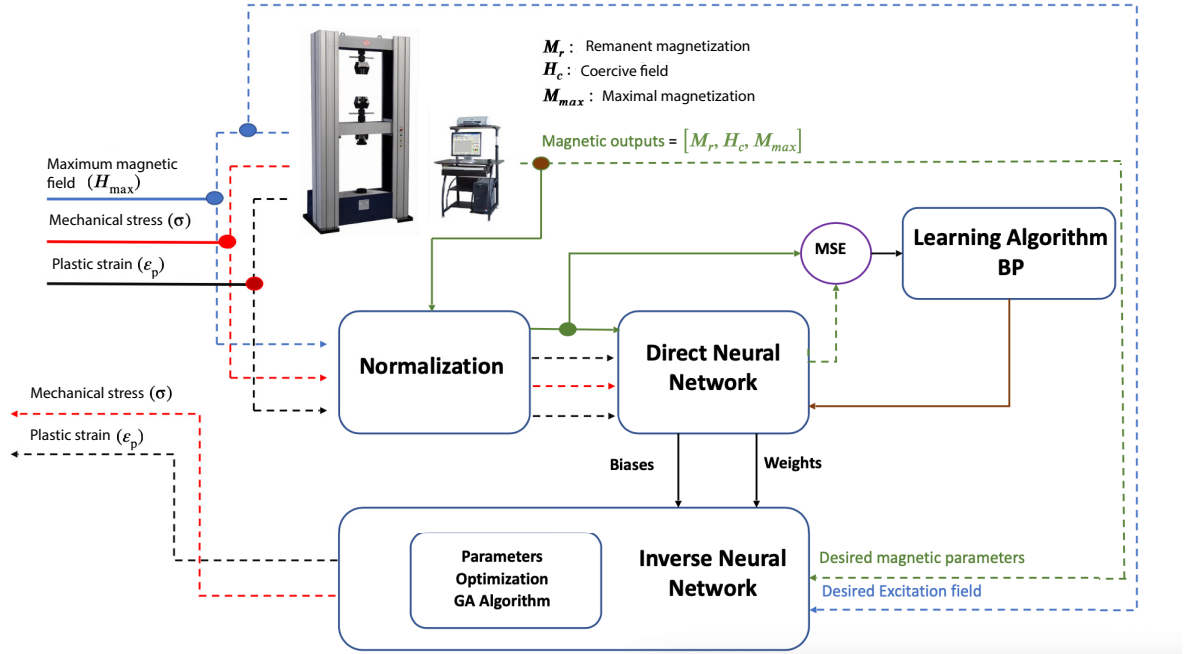


Figure 7: General overview of the proposed ANN-based modeling approach.

relation that is difficult to describe with physical models due to its ability to learn. Thus, the ANN can extract the existing relationship between the various variables that makes part of the application. Another relevant characteristic is its generalization ability: after a training process, the network is able to generalize the acquired knowledge, making possible to estimate unknown solutions of complex problems. ANN has been found to be relevant in many domains such as fracture mechanics [20], fatigue and failure analysis and detection [32]. Figure 7 depicts the ANN-based approach for the modeling of the influence of plastic deformation and applied stress on the magnetic behavior of ferromagnetic materials.

3.1. Dataset for ANN

As shown in the previous section, the variation of the remanent magnetization, coercive field and the maximum magnetization strongly depends on magnetic field strength (especially its maximal value), mechanical stress and plastic strain level. For that reason, the considered ANN model inputs/outputs are summarized in table 1. 672 (input,output) couples are provided from specimen A.

Table 1: ANN Model parameters

Input/output	variable	Units
In 1 : Maximal magnetic field	H_{max}	A/m
In 2 : Stress	σ	MPa
In 3 : Plastic strain	ϵ_p	%
Out 1 : Remanent magnetization	M_r	A/m
Out 2 : Coercive field	H_c	A/m
Out 3 : Maximal magnetization	M_{max}	A/m

The matrix below represents the entire dataset:

$$\begin{pmatrix} In_1 & In_2 & In_3 & Out_1 & Out_2 & Out_3 & \\ H_{1_{max}} & \epsilon_p^1 & \sigma_1 & M_{1_r} & H_{1_c} & M_{1_{max}} & D_1 \\ \vdots & \vdots & \vdots & \vdots & \vdots & \vdots & \vdots \\ H_{i_{max}} & \epsilon_p^j & \sigma_k & M_{i_r} & H_{j_c} & M_{k_{max}} & \vdots \\ \vdots & \vdots & \vdots & \vdots & \vdots & \vdots & \vdots \\ H_{I_{max}} & \epsilon_p^J & \sigma_K & M_{I_r} & H_{J_c} & M_{K_{max}} & D_{672} \end{pmatrix} \quad (1)$$

where :

$$H_{i_{max}} \in \begin{bmatrix} 230A/m & 450A/m & 680A/m & 1140A/m & 1300A/m \\ 1600A/m & 1800A/m & 2000A/m & 2200A/m & 5500A/m \\ 10300A/m & & & & \end{bmatrix} \quad (2)$$

and

$$\epsilon_p^j \in [0\% \quad 1\% \quad 2\% \quad 3\% \quad 5\% \quad 10\% \quad 15\% \quad 20\%] \quad (3)$$

Data are divided into three different subsets:

- The training set composed by 60% of the specimen A dataset;
- The **validation set** composed by 40% of specimen A the dataset;
- The **testing set** composed from measurements performed on specimen B (see Appendix A).

Before an ANN can be trained, all input and output data must be acquired and normalized. Indeed large input values combined with small ones in a learning algorithm can undermine the training phase. A normalization criterion shown in equation (4) has been used for input data, where y is the normalized input value and x the original value. The normalization interval used is $[0.01, 0.99]$. This criterion allows a normalization for both negative and positive values [33, 34].

$$y = y_{min} + \frac{x - x_{min}}{x_{max} - x_{min}}(y_{max} - y_{min}) \quad (4)$$

Normalization of output data x' is made by dividing the actual value by its maximum value as shown in the equation below:

$$y' = \frac{x'}{\max(x')} \quad (5)$$

3.2. ANN architecture

The analysis is conducted using the Keras library in Python 3.6. A parametric study is performed to determine the number of hidden layers and the number of neurons in each layer to be used to get an architecture which produces the lowest prediction error. Each hidden layer contains the same number of neurons. This choice allows for the reduction of parameters number that can be changed in the model [35]. In our system, the ANN is trained under mean-square-error (MSE) criterion with feed forward back-propagation algorithm (BP). Detailed description of the training process is given in Appendix B.

The gradient descent method could be used to optimize the cost function $J(X, d)$ (X : input data; d : desired output) with respect to weight vectors W_i (in example below, two weight vectors are considered). This method computes the derivative of the cost function as function of a given parameter for the entire training set. The weight vector that is used for the next step is calculated by :

$$W_i(n+1) = W_i(n) - \eta \frac{\partial J(X, d)}{\partial W_i(n)} \quad i = 1, 2 \quad (6)$$

where η is the learning rate of the algorithm (chosen between 0 and 1). This method requires computing the gradient of the whole training set to perform only one update step. A huge computational time is required to train the ANN for a large dataset. To reduce the computation time, the stochastic gradient descent (SGD) method could be adopted since it performs one parameter update for only one training example. The updating rule is given in Eq 7 :

$$W_i(n+1) = W_i(n) - \eta \frac{\partial J(X(n), d(n))}{\partial W_i(n)} \quad i = 1, 2 \quad (7)$$

However, SGD performs frequent updates with a high variance that causes the objective function to fluctuate dramatically [36]. Mini-batch gradient descent [37] finally takes the best of the two methods and performs an update at each mini-batch of one training example:

$$W_i(n+1) = W_i(n) - \eta \frac{\partial J(X(n:n+l), d(n:n+l))}{\partial W_i(n)} \quad i = 1, 2 \quad (8)$$

The batch size for this example is l . The parameter variance is reduced by this way at each update, which can lead to a more stable convergence. Nevertheless, this method has some limits that we need to be addressed. The choice of the learning rate η is difficult in many applications. Additionally, the same learning rate applies to all parameter updates, although we do not need to update all of

them the same way. It could be preferable to perform a larger update for rarely occurring features.

Adaptive Moment estimation (ADAM)[38] is an algorithm for gradient optimization that computes adaptive learning rates for each parameter. The algorithm updates exponential moving averages of the gradient (m_i^t) and the squared gradient (v_i^t) where the hyper-parameters $\beta_1, \beta_2 \in [0, 1]$ control the exponential decay rates of these moving averages. We compute m_i^t and v_i^t as follows:

$$m_i^t = \beta_1 m_i^{t-1} + (1 - \beta_1) g_i^t \quad i = 1, 2 \quad (9)$$

$$v_i^t = \beta_2 v_i^{t-1} + (1 - \beta_2) (g_i^t)^2 \quad i = 1, 2 \quad (10)$$

where :

$$g_i^t = \frac{\partial J(X(n : n + l), d(n : n + l))}{\partial W_i(n)} \quad i = 1, 2 \quad (11)$$

m_i^t and v_i^t are estimates of the first moment (average) and of the second moment (uncentered variance) of gradients. These biases are counteracted by computing bias-corrected first and second moment estimates as follows:

$$\hat{m}_i^t = \frac{m_i^t}{1 - (\beta_1)^t} \quad i = 1, 2 \quad (12)$$

$$\hat{v}_i^t = \frac{v_i^t}{1 - (\beta_2)^t} \quad i = 1, 2 \quad (13)$$

The updating rule is then :

$$W_i(n + 1) = W_i(n) - \frac{\eta}{\sqrt{\hat{v}_i^t + \epsilon}} \hat{m}_i^t \quad i = 1, 2 \quad (14)$$

ϵ is numerical parameter avoiding 0 at denominator ($\epsilon = 10^{-8}$). In this work, the ADAM algorithm is used to optimize the following objective function :

$$MAPE = \frac{1}{n} \sum_{i=1}^n \left| \frac{Y_i - R_i}{R_i} \right| \quad (15)$$

$$MSE = \frac{1}{n} \sum_{i=1}^n (Y_i^2 - R_i^2) \quad (16)$$

Where Y_i are the experimental values and R_i are the predicted ones.

Many tests have been performed to find the best configuration. We conducted tests using *softplus* and *softsign* activation functions which are given for input data x by :

$$Softplus(x) = \ln(1 + e^x) \quad (17)$$

$$Softsign(x) = \frac{1}{1 + |x|} \quad (18)$$

Table 2: Examples of tested ANNs configurations

Config. number	Number of neurons	Number of hidden layers	Epochs	training data		testing data	
				MAPE	MSE	MAPE	MSE
1	8	1	500	34.21	0.022	28.38	0.03
2	16	1	500	33.87	0.021	27.27	0.02
3	64	1	500	33.03	0.019	24.77	0.02
4	16	2	500	24.71	0.0086	18.23	0.01
5	16	2	1000	18.53	0.0059	14.91	0.01
6	64	2	1000	15.20	0.004	12.88	0.008
7	64	3	1000	9.32	0.0018	7.60	0.003
8	64	3	1500	5.57	0.001	6.32	0.0027
9	64	4	1500	5.26	6.7e-04	3.71	8.8e-04

Three hyper parameters (number of hidden layers, number of neurons in each layer and Epochs) have been adjusted in order to get an optimized ANN.

Table 2 illustrates a set of tested configurations and associated errors calculated from training and testing data. The fourth column indicates the number of *Epochs*. ~~It is the number of times the ANN trains the weights for each neuron to optimize the outputs from the given input sets~~ **In each epoch the ANN is trained with all the training data.**

9 configurations are gathered in this table using the same activation function *Softplus*. We see that the 9th configuration gives a significant error reduction. This configuration requires nevertheless 1500 Epochs and we observe that MAPE objective function is lower for testing data than for training data, which corresponds to an under-fitting situation. A so-called early stopping procedure has been applied to choose the number of Epochs: early stopping is a method that allows for the specification of an arbitrary large number of training Epochs. A stop number is activated once no error improvement is observed for a validation dataset The optimized architecture that has been chosen is finally composed of three hidden layers and 64 neurons per layer. Figure 8 shows the architecture of the final ANN.

3.3. ANN asymptotic conditions

Some physical constraints have been added. They allow solutions to remain in an acceptable range whatever the loading. For example, magnetization should not exceed the saturation magnetization of the material which is a physical limit. We then propose the following constraints:

- concerning magnetic loading, we define:

$$M(H) \approx M_c \quad \text{for} \quad H_{max} \rightarrow \infty \quad (19)$$

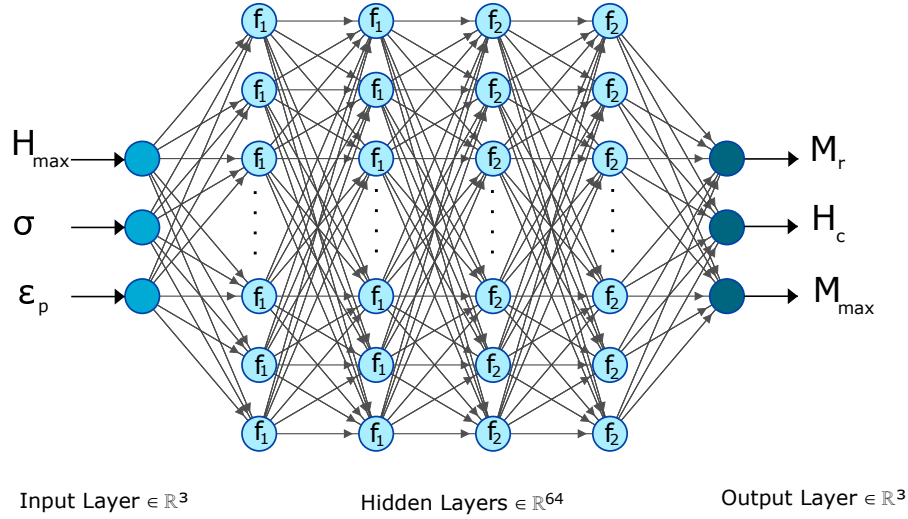


Figure 8: Architecture of the adopted MLP ANN.

Table 3: boundary conditions

@ Plastic strain interval	σ_{max,ϵ_p} (MPa)
$\epsilon_p < 3\%$	600
$3 < \epsilon_p < 10\%$	800
$10 < \epsilon_p \%$	1000

where M_c is a magnetization level, high enough to be considered as the magnetization at saturated state. We choose the magnetization obtained for $H_{max} = 10300 A/m$. The following behavior is added to ANN process :

$$M(H, \epsilon_p, \sigma) = M(10300, \epsilon_p, \sigma) \quad \text{when } H > 10300 A/m \quad (20)$$

- In addition, experiments show that magnetization tends to a different limit according to the mechanical loading. Some stress thresholds σ_{max,ϵ_p} depending on plastic strain level have been defined that allows a correct magnetization prediction to be obtained when $\sigma \rightarrow \infty$:

$$M(H, \epsilon_p, \sigma) = M(H, \epsilon_p, \sigma_{max,\epsilon_p}) \quad \text{when } \sigma > \sigma_{max,\epsilon_p} \quad (21)$$

σ_{max,ϵ_p} values are gathered in table 3.

4. Inversion of Feedforward Neural Networks

An efficient ANN is a very interesting tool because it makes an inversion of the process possible: to obtain a set of inputs from the knowledge of the

outputs. Applied to the data of the problem, it would become possible to estimate a mechanical state from magnetic measurements, reaching the possible objectives of a magnetic NDT procedure.

The neural network model is shown in figure 8. Outputs are given by the following set of equations:

$$L_{1,k} = f_1\left(\sum_{r=1}^R x_r w_{rk} + b_{1,k}\right) = \frac{\sum_{r=1}^R x_r w_{rk} + b_{1,k}}{1 + \left|\sum_{r=1}^R x_r w_{rk} + b_{1,k}\right|} \quad (22)$$

$$L_{2,k} = f_1\left(\sum_{s=1}^S L_{1,s} w_{sk} + b_{2,k}\right) = \frac{\sum_{s=1}^S L_{1,s} w_{sk} + b_{2,k}}{1 + \left|\sum_{s=1}^S L_{1,s} w_{sk} + b_{2,k}\right|} \quad (23)$$

$$L_{3,k} = f_2\left(\sum_{s=1}^S L_{2,s} w_{sk} + b_{3,k}\right) = \ln(1 + e^{\sum_{s=1}^S L_{2,s} w_{sk} + b_{3,k}}) \quad (24)$$

$$L_{4,k} = f_2\left(\sum_{s=1}^S L_{3,s} w_{sk} + b_{4,k}\right) = \ln(1 + e^{\sum_{s=1}^S L_{3,s} w_{sk} + b_{4,k}}) \quad (25)$$

$$y_i = f_2\left(\sum_{s=1}^S L_{4,s} w_{sk} + b_{5,i}\right) = \ln(1 + e^{\sum_{s=1}^S L_{4,s} w_{sk} + b_{5,i}}) \quad (26)$$

Subscript R is the number of neurons in the input layer. Subscript S is the number of neurons in the hidden layers. f_1 is the *Softsign* transfer function; f_2 is the *Softplus* transfer function; w and b are weights and the biases respectively.

In order to calculate the input vector $X(x_1, x_2, x_3) = (\sigma, \epsilon, H_{max})$ corresponding to the output vector $Y(y_1, y_2, y_3) = (M_r, H_c, M_{max})$, we need to define an objective function to optimize the input vector and an optimization algorithm. We then define the variable Z as the absolute value of the difference between the output of the ANN Y_{out} and the desired magnetic vector $d(d_1, d_2, d_3)$.

$$Z_i = |y_i - c_i| \quad i \in [1, 2, 3] \quad (27)$$

The objective function F is then :

$$F(X) = \sqrt{Z_1^2 + Z_2^2 + Z_3^2} = \sqrt{(y_1 - d_1)^2 + (y_2 - d_2)^2 + (y_3 - d_3)^2} \quad (28)$$

It can be rewritten as:

$$F(x_1, x_2, x_3) = \sqrt{\sum_{i=1}^{i=3} (\ln(1 + e^{\sum_{s=1}^S L_{4,s} w_{sk} + b_{5,i}}) - c_i)^2} \quad (29)$$

the third variable x_3 which represents the maximum magnetic field is considered known. The optimization is then restricted to x_1 and x_2 which are the stress

and the plastic strain, respectively. The optimization problem can be stated as follows :

$$\begin{aligned} (\epsilon_p, \sigma)_{opt} &= \arg \min F(X) \\ \text{subject to : } & -300 \leq \sigma(i) \leq 800 \quad (\text{MPa}) \\ & 0 \leq \epsilon_p(i) \leq 25\%, \forall i \in \mathbb{N} \end{aligned} \quad (30)$$

The Nelder-mead method (NM) and the Genetic algorithm (GA) are used to optimize this function. Those algorithms have the particularity to minimize a function without calculating the gradient of the function, which is time consuming because of the complexity of the objective function.

5. Methodology for multivariable function optimization

As shown in equation (26), ANN model can be expressed as a multivariable function. This section describes thus the meta-heuristic algorithms used to solve this multivariable function.

5.1. Nelder-mead algorithm

The Nelder-Mead (NM) method is a widely used nonlinear optimization algorithm. This numerical method allows for the minimization of an objective function in a multi-dimensional space [39]. This algorithm is a direct search method that does not use numerical or analytic gradient [40]. NM method involves 5 steps: *sorting*, *reflection*, *expansion*, *contraction* and finally *shrinkage* [41]. Figure 9 illustrates the algorithm flowchart.

In this algorithm, the initial $n+1$ vertices are first generated (X_1, X_2, \dots, X_{n+1}) where $X_i = (\sigma, \epsilon_p)_i$ and the objective function values $F(X_i)$ are evaluated. The computed fitting functions are then compared and sorted and the following states are determined : the best X_b , the worst X_h , the next worst X_{nw} and the centroid points \bar{X} . These points are calculated using four adjustment scalar coefficients named as reflexion (α), expansion (γ), contraction (β). After the initializing and sorting steps, the reflexion point X_r is calculated as follows:

$$X_r = \bar{X} + \alpha(\bar{X} - X_h) \quad (31)$$

Similarly, the expansion point X_e is determined as follows :

$$X_e = \bar{X} + \gamma(X_r - \bar{X}) \quad (32)$$

X_e replaces the worst value X_h if the lowest value of the expansion point is smaller than that of the reflexion point (X_r replaces X_h). If $F(X_r) > F(X_{nm})$, the contraction step is applied. An outside contraction (*oc*) is applied when $F(X_r) < F(X_h)$ and X_{oc} is calculated as :

$$X_{oc} = \bar{X} + \beta(X_r - \bar{X}) \quad (33)$$

If $F(X_{oc}) < F(X_r)$, X_h is replaced by X_{oc} and this completes the iteration. Otherwise, we move to next step which is denoted as shrinkage.

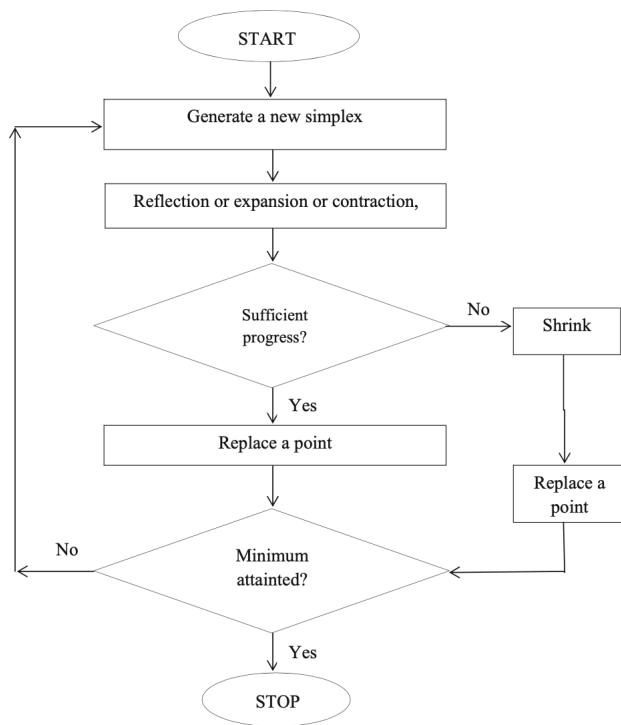


Figure 9: Nelder Mead flowchart [42]

Table 4: Nealder-mead algorithm parameters

n	Reflexion (α)	Contraction (β)	Expension (γ)
3	1	0.5	2

If $F(X_h) < F(X_r)$, the inside contraction (*ic*) is applied and X_{ic} is calculated using the equation below:

$$X_{ic} = \bar{X} + \beta(X_h - \bar{X}) \quad (34)$$

If $F(X_{ic}) < F(X_h)$ then X_h is replaced by X_{ic} . Else, the shrinkage occurs. The shrinkage is the final step in NM algorithm which uses the equation below to construct new points by *shrinking* them.

$$X_i = X_i + \gamma(X_b - X_i) \quad i = 2, 3, \dots, n + 1 \quad (35)$$

The numerical algorithm of the NM simplex method has been described in detail by Nelder and Mead [43]. Table 4 gathers the chosen NM parameters.

5.2. Genetic algorithm

Genetic Algorithms (GAs) are a set of computational algorithms inspired by the evolution of species. These algorithms encode the potential solutions for a specific problem in an individual data structure. This possible solution looks like a chromosome to which a recombination is applied by the genetic operators, conserving genetic information as a possible solution in the individuals of the next generation [44]. The GA is organized by three operators: reproduction, crossover, and mutation. The new population is created after the application of the three steps. This process is iterated until attending the chromosome which minimizes the objective function and can consequently be considered as the optimal solution.

The process is started by creating randomly a population with N individuals. Each individual is called chromosome $X_i = (x_1, x_2, \dots, x_n)$ where n is the number of parameters to be optimized (in our case, $X_i = (\sigma, \epsilon_p)_i$). Next, population is evaluated using the objective function; this evaluation constitutes the initial fitting vector. Let define P as the population :

$$P = [X_1, X_2, \dots, X_N] \quad (36)$$

For each chromosome X_i in population P , three other vectors X_j , X_k and X_l are selected with $j \neq k \neq l \neq i$. X_i is the target vector. The three vectors are randomly chosen from the population without replacement. The three vectors (X_j , X_k and X_l) are combined to create a new chromosome called the mutant chromosome. The mutant vector is calculated as :

$$X_{mut} = X_j + \mu(X_k - X_l) \quad (37)$$

Table 5: Genetic algorithm parameters

Population size (N)	Number of parameters (n)	μ	p
40	2	0.8	0.7

where μ is a mutation factor.

The recombination is the next step after calculating the mutant vector. It consists in mixing the mutant vector with the current vector to create a new trial chromosome X_{cr} . To do that, some elements of the current vector have been mixed with elements of the mutant vectors. Considering Y_j as the random variable able to change $X_i(j)$ in the actual vector X_i , Y_j follows the Bernoulli trials with a probability of success p . We then have :

$$Z = Y_1 + Y_2 + \dots + Y_n \quad (38)$$

Z follows a binomial distribution with parameters n and $p \in [0, 1]$. The probability weight function of Z is given by :

$$f = \binom{n}{k} p^k (1-p)^{n-k} \quad k = 0, 1, \dots, n \quad (39)$$

After new trial vector obtention, a new F value is calculated: if $F(X_{cr}) > F(X_i)$, the target vector X_i is preserved; if $F(X_{cr}) < F(X_i)$, X_i is replaced by X_{cr} . All these steps are repeated for the whole population. This completes the first iteration of the algorithm. Values of parameters used for our testing case are gathered in table 5.

6. Results and discussion

6.1. Cross validation

This section gathers some comparisons between experimental H_c , M_r and M_{max} results as function of stress and plastic strain, and the modeling results from ANN after processing. Figures 11a to 11c allow for a visual comparison between predicted values and target (experimental) values. This corresponds to the validation step of the procedure. First the *cross validation* has been applied. This validation method is useful for machine learning when data amount is relatively small [45]. In k -fold cross-validation the data is first partitioned into k equally sized folders as illustrated in figure 10. Subsequently k training iterations and validation are performed so that within each iteration, a different data folder (one of the k folders) is held-out as a testing set while the remaining $k - 1$ folders are used for learning. Finally all data are used as a validation set one time at least [46]. The model accuracy has been evaluated using $k = 5$. Table 6 summarizes MAPE obtained for each folder. The model exhibits an accuracy of about 91% and a MAPE of about 3.7 %.



Figure 10: Schematic diagram of cross validation method. [46]

Table 6: Accuracy calculated for the five folders

	Folder 1	Folder 2	Folder 3	Folder 4	Folder 5
MAPE (%)	4.01	3.01	5.04	3.70	3.43
Accuracy (%)	90.0	92.9	90.0	91.3	91.0

The next step is model evaluation, which is major step in assessing the performance of any machine learning model. The predicted values are compared with observed ones (in our case observed values are the result of physical experiments using specimen B - see Appendix A). The specimen is loaded in the same conditions as the previous one. We propose a step-by-step comparison, making gradually more complex the mechanical loading.

6.2. Effect of applied stress (without plastic strain)

The model was first applied to data collected under stress in the elastic domain ($\epsilon_p = 0$). Let F_{ANN} be the model function. We then have :

$$\begin{cases} F_{ANN}^{i,k,j} = F_{ANN}(\sigma_i, \epsilon_p = 0, H_j^{max}), & i \in [1, 7], k \in [1, 3], j \in [1, L] \\ \text{with } F_{ANN}^{i,1,j} = M_r, F_{ANN}^{i,2,j} = H_c, F_{ANN}^{i,3,j} = M_{max} \end{cases} \quad (40)$$

Input datas are: $H_j^{max} \in [0 : 0.1 : 14e3]$ A/m, $\sigma_i \in [-200, -40, 0, 40, 120, 200]$ MPa, $\epsilon_p = 0$ and $L = length(H_{max}) = 140.10^3$. Predicted values of remanent magnetization, coercive field and maximal magnetization are compared to experimental values collected from specimen B.

Figure 12a shows the variation of remanent magnetization according to the maximum applied magnetic field and for seven applied stress levels (-200 MPa, -40 MPa, 0 MPa, 40 MPa, 120 MPa, 200 MPa). We observe a good general agreement between experimental measurements and model. The highest discrepancies are observed for $\sigma = 120MPa$, highlighting some difficulties to model the Villari reversal. Prediction of remanent magnetization under applied stress for $H_{max} > 10^4 A/m$ seems relevant even if the training data was limited

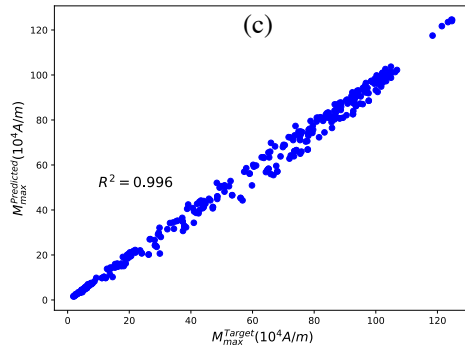
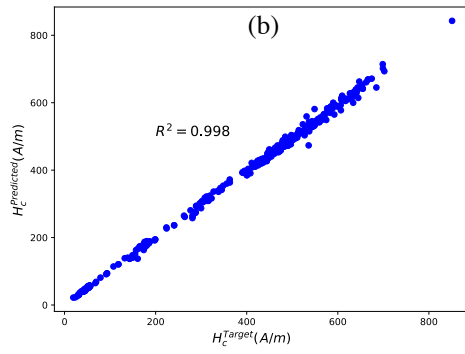
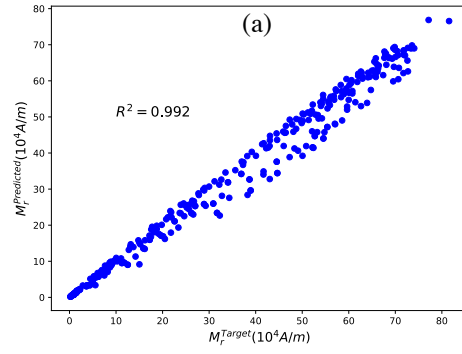


Figure 11: Comparison between observed and predicted target data: (a) remanent magnetization; (b) coercive field; (c) maximal magnetization

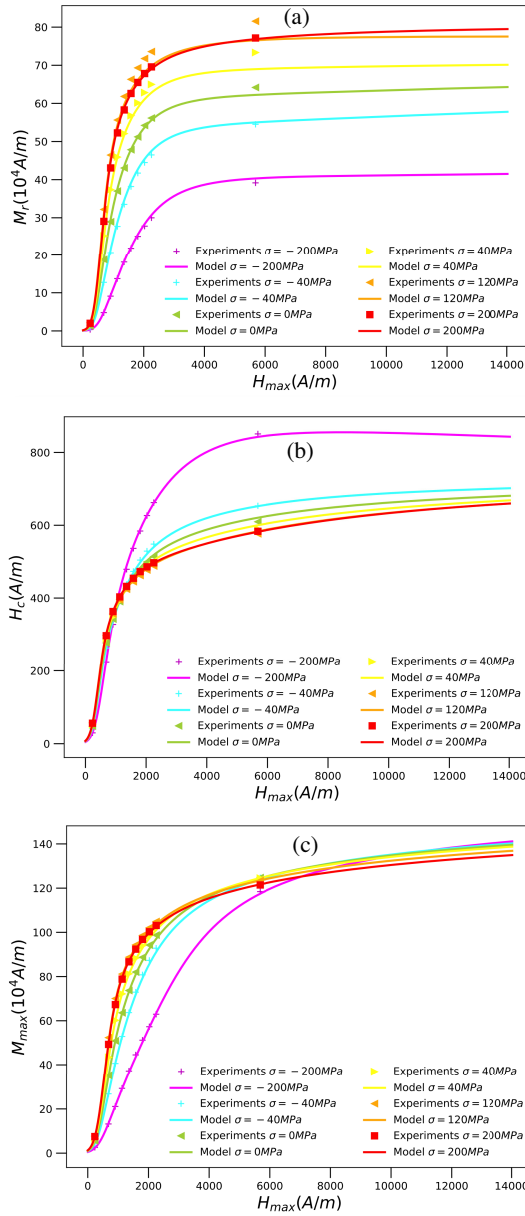


Figure 12: Comparison measured-predicted values for specimen B: (a) remanent magnetization; (b) coercive field; (c) maximum magnetization

to $H_{max} = 10^4 A/m$. This highlights the effect of physical constraints that have been implemented in the algorithm. Figure 12b allows for a comparison between experimental and modeled coercive field. Coercive field variations seem accurately modeled for all stress levels. It tends to saturate at high magnetic field strength. A slight decrease is observed for $\sigma=200\text{MPa}$ curve when magnetic field reaches its highest value. Experimental and modeled variations of maximum magnetization with magnetic field are illustrated in figure 12c. Very small discrepancies are observed and approach to physical saturation sounds relevant. This first set of validation comparisons, obtained under applied stress without plastic strain are very satisfying.

A 2D representation of modeling results for remanent magnetization, coercive field and maximal magnetization is proposed in figure 13, allowing for a better observation of variations and gradients. The following range has been used:

$$\sigma_i \in [-300 : 1 : 300]\text{MPa} \quad H_j^{max} \in [0 : 1 : 5000]\text{A/m}$$

We can see in figure 13a that remanent magnetization increases with tensile stress for a maximum magnetic field higher than 2000A/m until a threshold is reached. Remanent magnetization then begins a slight decreasing. This behavior is in accordance with experimental results and seems to correspond to a Villari effect. The highest remanent magnetization values are obtained for $\sigma \approx 150\text{MPa}$. In compression, gradients show that remanent magnetization seems more magnetic field sensitive than stress sensitive. Fig 13b shows that the strongest variations and strongest values of coercive field are obtained under compression at high magnetic field. Even if this result is in accordance with experiments attention must be paid to a possible divergence of the model for higher magnetic field and compression. H_c decreases when $\sigma > 0$ and saturation seems occurring at increasing maximum applied field levels. In tension, gradients show that coercive field seems more magnetic field sensitive than stress sensitive. Variations of maximum magnetization plotted in figure 13c look close to variations of remanent magnetization. The maximum values are reached for $\sigma \approx 50\text{MPa}$ and at high magnetic field. The decreasing of maximum magnetization with stress at high magnetic field is symptomatic of Villari reversal. Variations with magnetic field under compression are stronger than for remanent magnetization.

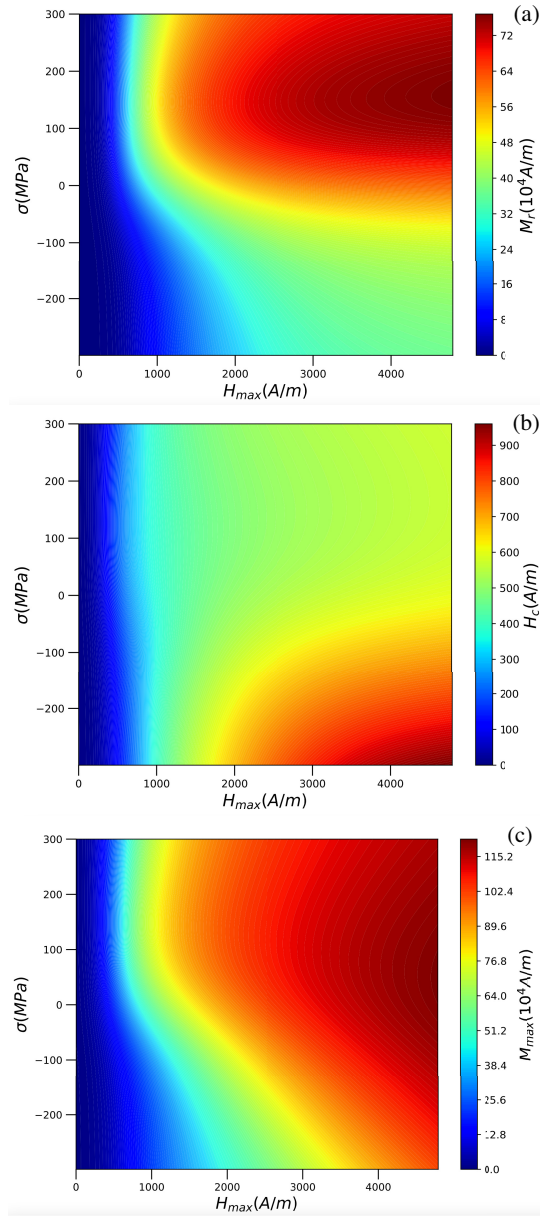


Figure 13: (a) Predicted remanent magnetization according to σ and H_{max} ; (b) predicted coercive field according to σ and H_{max} ; (c) predicted maximum magnetization according to σ and H_{max} .

6.3. Effect of plastic straining (without applied stress)

Data collected for plastic strained sample at the unloaded state ($\sigma = 0$ MPa) are used. We then have :

$$F_{ANN}^{i,j} = F_{ANN}(\sigma = 0, \epsilon_{pj}, H_i^{max}), \quad i \in [1, 3], j \in [1, L] \quad (41)$$

with $\epsilon_{pj} \in [0 : 0.01 : 24]\%$, $H_i^{max} \in [230, 1000, 2000]$ A/m and $L = \text{length}(\epsilon_p) = 2401$

It must be first noticed that plastic strain range is wider than the experimental range used for training ($\max(\epsilon_p)=20\%$). This extension can be used as a test for model learning capacity.

Figures 14a-c illustrate the remanent magnetization variations according to plastic strain for the three maximum magnetic field levels. Remanent magnetization decreases as expected and a very good agreement is observed between experimental points and modeling. Predictions for plastic strain higher than 20% seems relevant too, highlighting a progressive expected saturation.

Figures 15a-c show experimental and modeled variations of coercive field versus plastic strain for the three maximum magnetic field levels. As previously discussed, variations of coercive field with plastic strain at low field and high field are opposite: H_c decreases strongly according to the plastic strain in the first stages of deformation (0% to 5%) and it tends to saturate for higher plastic strain. H_c increases on the contrary according to plastic deformation at high magnetic field (figure 16c), when $0\% \leq \epsilon_p \leq 5\%$ and it saturates after a small decreasing. Coercive field vs plastic strain exhibits a non-monotony at intermediate magnetic fields: it increases at low plastic strain level then it decreases drastically at higher levels.

Figures 16a-c show experimental and modeled variations of maximum magnetization versus plastic strain ϵ_p . As for applied stress without plastic strain, variations of maximum magnetization follows approximately variations of remanent magnetization. Some increasing with plastic strain is observed at low magnetic field (figure 16a). This variation is not reproduced by the modeling but may be considered as a measurement error. For all magnetic field levels, the maximum magnetization tends to saturate for $\epsilon_p > 20\%$.

For all situations, the ANN model gives very good estimations, underlining its ability to model such a very complex behavior.

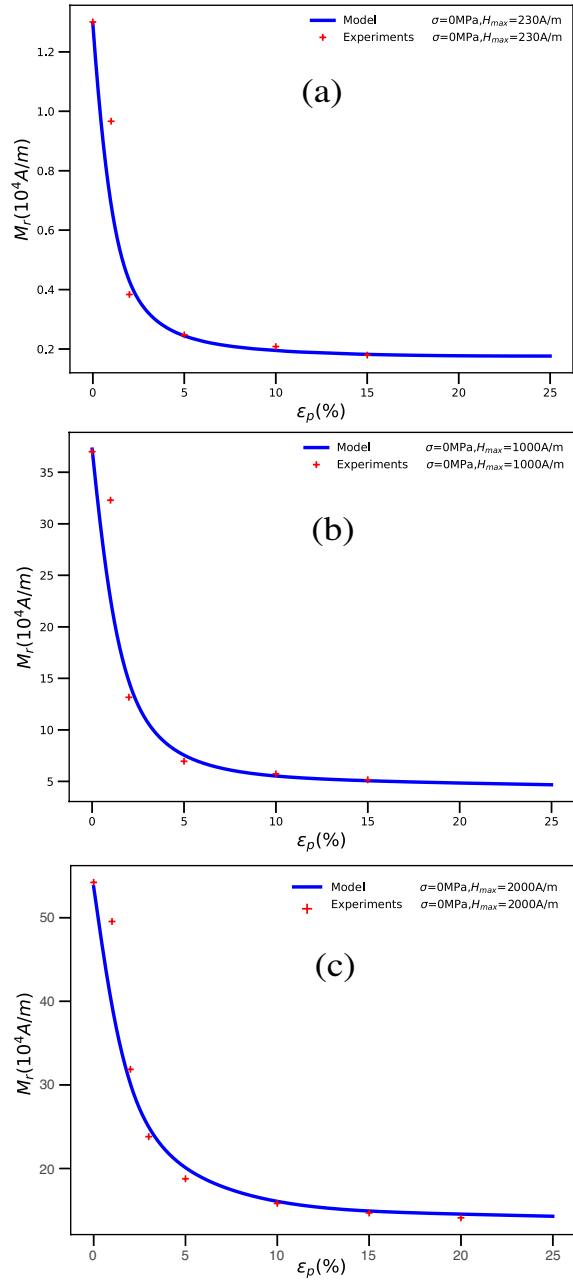


Figure 14: Comparison measured/predicted values of the remanent magnetization as function of plastic strain level at different maximal magnetic field strength: (a) 230A/m; (b) 1000A/m; (c) 2000A/m - (no applied stress $\sigma = 0$).

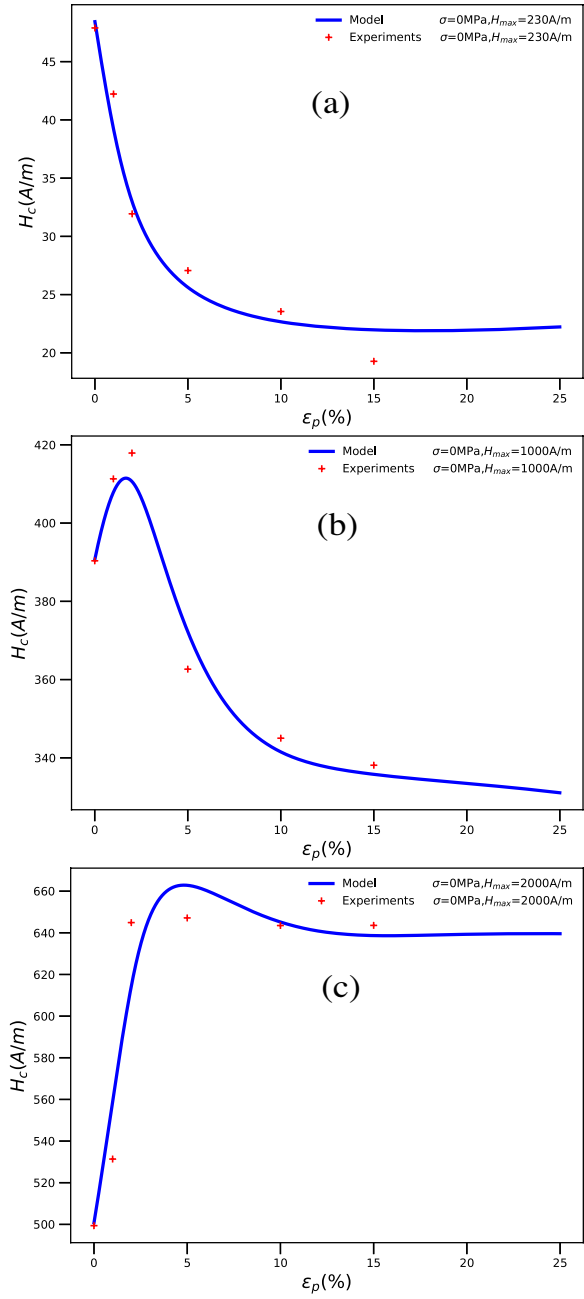


Figure 15: Comparison measured/predicted values of coercive field as function of plastic strain level at different maximal magnetic field strength:(a) 230A/m; (b) 1000A/m; (c) 2000A/m - (no applied stress $\sigma = 0$).

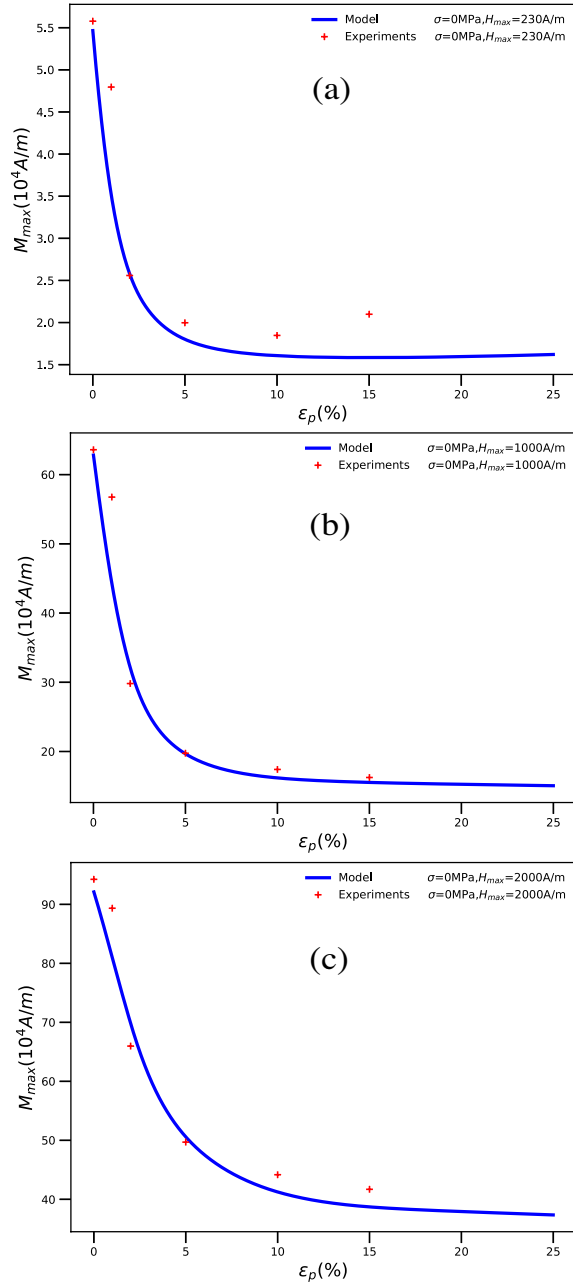


Figure 16: Comparison measured/predicted values of maximum magnetization as function of plastic strain level at different maximal magnetic field strength: (a) 230A/m; (b) 1000A/m; (c) 2000A/m - (no applied stress $\sigma = 0$).

6.4. Effect of plastic straining under mechanical loading

In this section, the model was evaluated as follows :

$$F_{ANN}^{i,l,j} = F_{ANN}(\sigma_j^i, \epsilon_{pi}, H_l^{max}), \quad i \in [1, 8], l \in [1, 6], j \in [1, L_i] \quad (42)$$

where :

$$\sigma_j^i \in [\sigma_{inf}^i : 0.01 : \sigma_{sup}^i]$$

$$\epsilon_{pi} \in [0, 1, 2, 3, 5, 10, 15, 20](\%)$$

$$H_l^{max} \in [230, 450, 680, 1340, 1560, 2000](A/m)$$

$$L_i = length(\sigma_j^i)$$

Figures 17a to 17f allow for a comparison between experimental and modeled estimations of remanent magnetization as function of plastic strain level and stress amplitude at the six maximum magnetization field strength. Each curve defines the remanent magnetization variation as function of stress for a given plastic strain level. The modeling accurately follows the remanent magnetization variations including the non-monotony at high stress and some crossings. The model overestimates nevertheless slightly the remanent magnetization at low plastic strain level for low maximum magnetic field conditions whereas it is underestimated for high maximum magnetic field conditions. Saturations for high compressive stress look suitable for all situations. Saturation is not reached under tension but tendencies seem relevant too, in accordance with experimental results. Figures 18a to 18f allow for a comparison between experimental and modeled estimations of remanent magnetization as function of plastic strain level and stress amplitude at the six maximum magnetization field strength. The variations of coercive field approximately follow those of the remanent magnetization for a maximum magnetic field up to 450A/m (figures 18a and 18b): increasing of the coercive field under stress up to a threshold where the coercive field begins to decrease. Plastic deformation gradually reduces the coercive field leading to relatively parallel curves. As the maximum magnetic field increases, trends completely change: the gradually increasing stress leads to a reduction of the coercive field (which results in an increasing number of curves crossing), but an increasing plastic deformation leads on the contrary to a higher coercive field. It is very interesting to observe that reversals and gradual shift of stress crossing point to lower values are accurately modeled. The model thus predicts a reversal of trends under compression for the two highest maximum magnetic fields (figures 18e and 18f). Figures 19a to 19f illustrate the predicted maximum magnetization M_{max} compared to experimental values. Each curve define the maximum magnetization variation as function of stress for a given plastic strain level. Model and experiments look in agreement whatever the situation. Discrepancies are observed for the same loading conditions as discrepancies observed for remanent magnetization. Maximum magnetization variations are indeed very close to remanent magnetization variations, highlighting saturation under compression and Villari reversal. These elements of

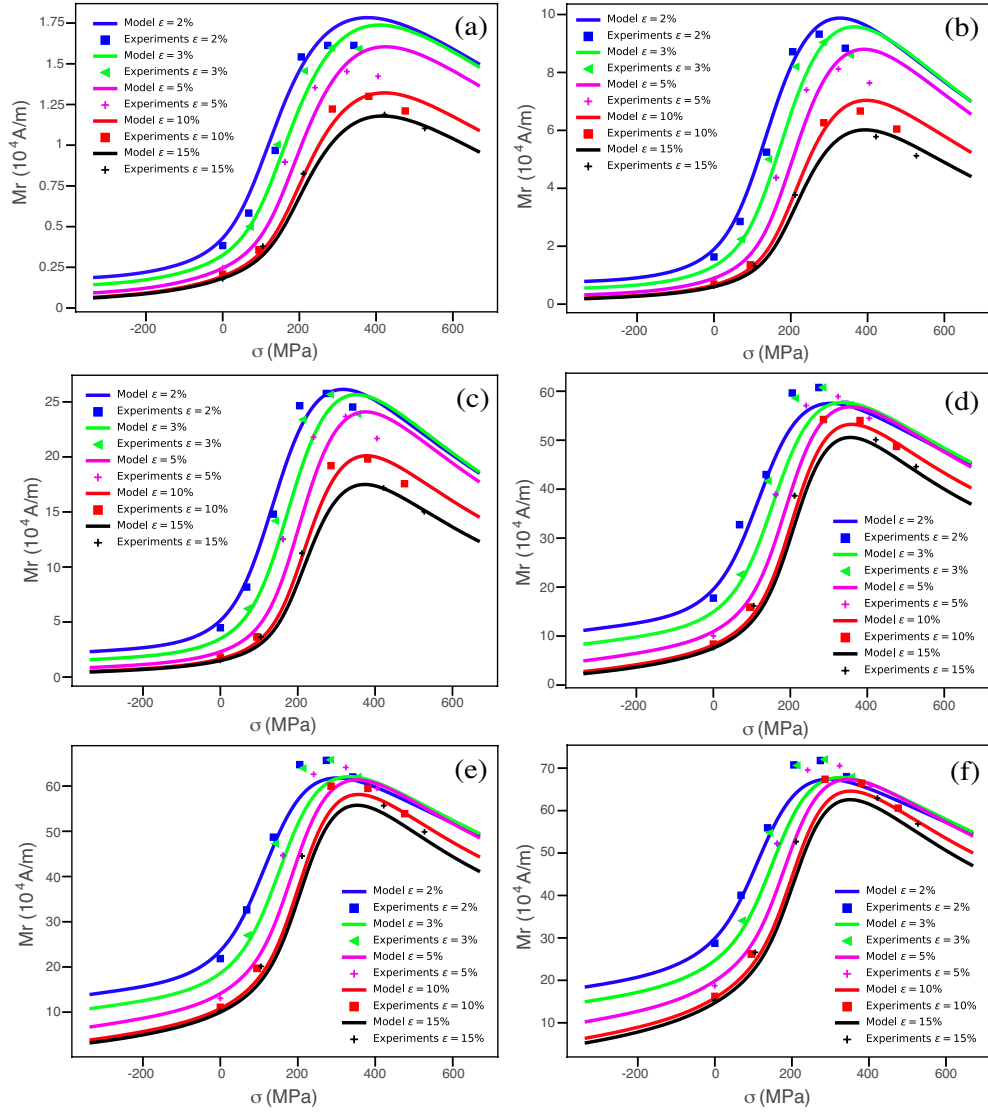


Figure 17: Comparison measured-predicted values of remanent magnetization for deformed specimen B : (a) $H_{max} = 230$ A/m; (b) $H_{max} = 450$ A/m; (c) $H_{max} = 680$ A/m; (d) $H_{max} = 1340$ A/m; (e) $H_{max} = 1560$ A/m; (f) $H_{max} = 2000$ A/m

comparisons make it possible to conclude that the ANN model is quite able to model the combined influence of plasticity and uniaxial stress. Note that the model was identified using measurements obtained on a first specimen (specimen A) while the validation tests use measurements obtained with a second specimen (specimen B). No model to our knowledge can reach such a level of prediction.

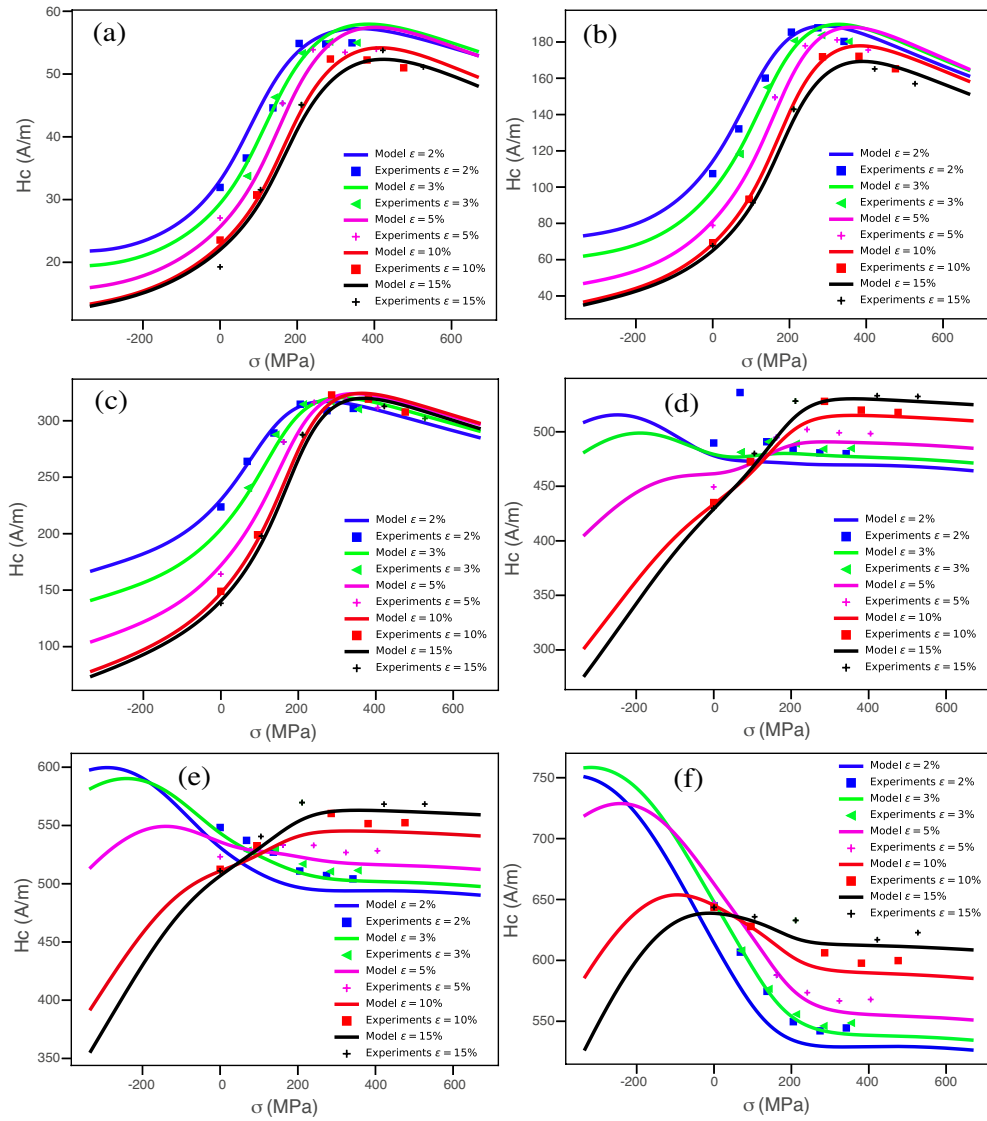


Figure 18: Comparison between measured and predicted values of coercive field for deformed specimen B as function of applied stress: (a) $H_{max} = 230A/m$; (b) $H_{max} = 450A/m$; (c) $H_{max} = 680A/m$; (d) $H_{max} = 1340A/m$; (e) $H_{max} = 1560A/m$; (f) $H_{max} = 2000A/m$

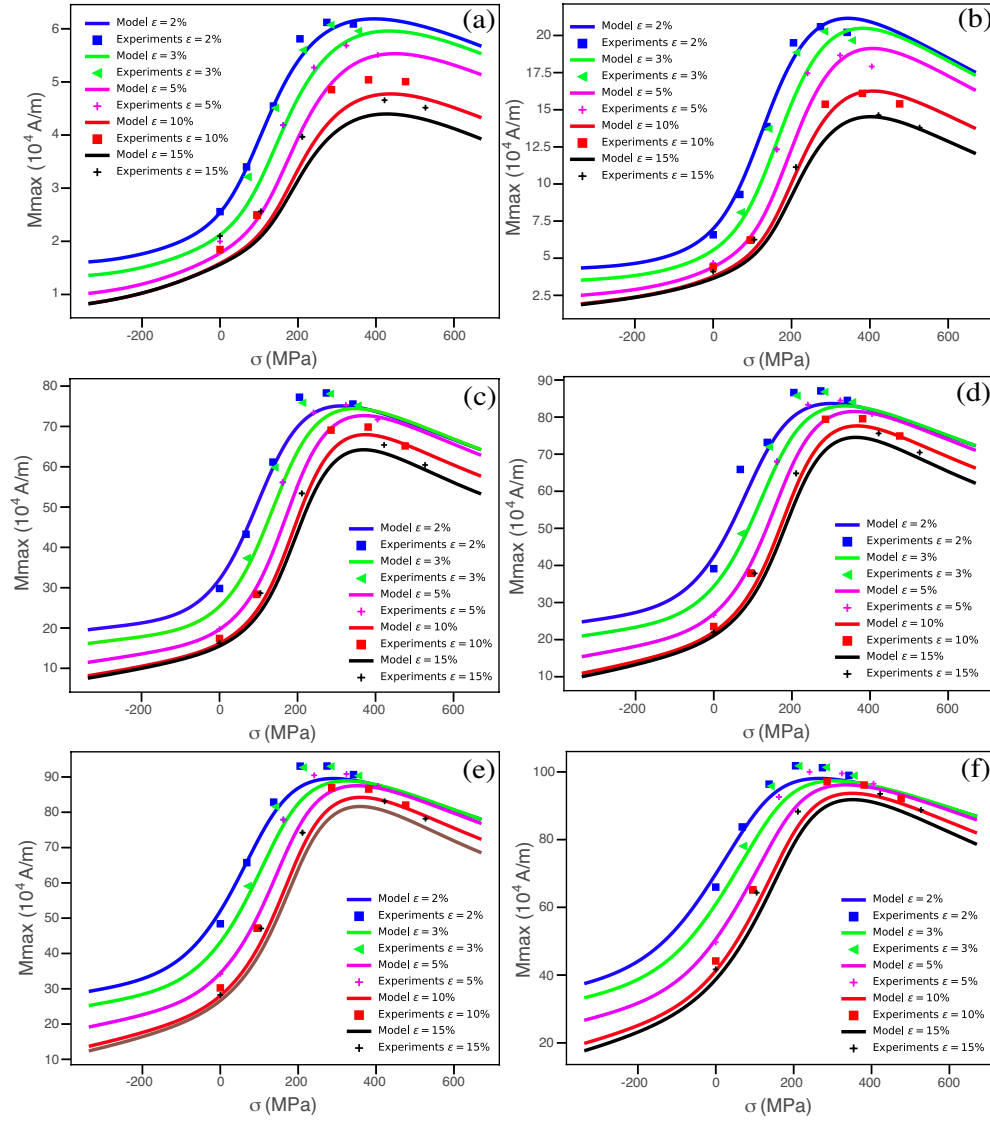


Figure 19: Comparison between measured and predicted values of maximum magnetization for deformed specimen B as function of applied stress: (a) $H_{max} = 230A/m$; (b) $H_{max} = 450A/m$; (c) $H_{max} = 680A/m$; (d) $H_{max} = 1340A/m$; (e) $H_{max} = 1560A/m$; (f) $H_{max} = 2000A/m$.

6.5. Inverse identification

This part illustrates how it is possible to use the ANN model to reach an inverse identification of mechanical state $M(\epsilon_p, \sigma)$ (supposed unknown) based on the magnetic signature $S(M_r, H_c, M_{max}, H_{max})$ (supposed known). Let F_{inv} defined in eq. (29) be the objective function to optimize. Table 7 gathers

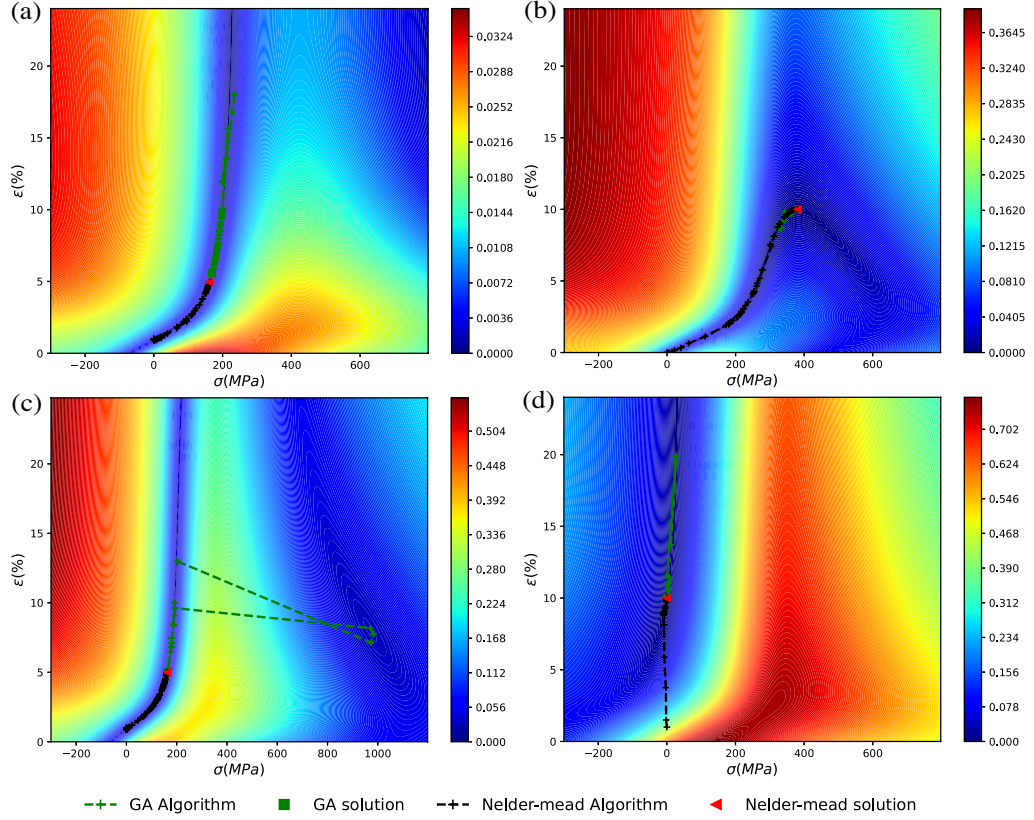


Figure 20: Inverse identification using NelderMead and Genetic algorithm: (a) S^1 ; (b) S^2 ; (c) S^3 ; (d) S^4

four situations (S^i) corresponding to four "virtual" magnetic signatures. Table 8 indicates in the two first columns the target quantities: *true* plastic stain and stress levels associated with the magnetic signatures in table 7. The next columns indicate the results of inverse identification using the GA and NM algorithms respectively (process is initiated with solutions: $\epsilon_p = 0\%$ and $\sigma = 0\text{MPa}$ for NMA; GA does not need any initialization). N indicates the number of iterations required for identifications. Figures 20a to 20d illustrate the objective function evaluated for $\epsilon_p = [0 : 1 : 25]\%$ and $\sigma = [-300 : 1 : 800]\text{MPa}$ and show the path used for GA and NMA to obtain the optimized solution for the four situations. We focus first on figure 20a that shows how F_{inv} evolves for the first magnetic signature S^1 . NM algorithm gives $(\epsilon_p, \sigma) = (4.9\%, 161.6\text{MPa})$ after 76 iterations whereas GA gives $(\epsilon_p, \sigma) = (5.5\%, 169.0\text{MPa})$ after 147 iterations. Both estimations are very close to the target quantities: $(5\%, 162\text{MPa})$. NMA looks however more performant than GA. Figure 20b illustrates the objective function for signature S^2 . Both algorithms converge to the exact solution after 62 iterations for GA and after 88 iterations for NMA. GA is more performant

Table 7: Inverse identification 1rst step - magnetic signatures.

Magnetic signatures	H_{max}	M_r	H_c	M_{max}
S^1	230	0.73	43	3.33
S^2	674	20.1	324	35.2
S^3	1558	34.4	525	66.8
S^4	2000	15.6	646	41.2
unit	A/m	10^4 A/m	A/m	10^4 A/m

Table 8: Inverse identification 2nd step - estimation of mechanical quantities and iterations number N.

Mechanical quantities	Meas.		GA			NM		
	ϵ_p	σ	ϵ_p	σ	N	ϵ_p	σ	N
S^1	0	-120	0	-120	8	0	-120	4
S^2	10	381	10	381	62	10	381	88
S^3	5	162	5.5	169	115	4.9	162	113
S^4	10	0	10	0	72	10	0	48
unit	%	MPa	%	MPa	-	%	MPa	-

this time. Figures 20c and 20d illustrate the two last situations leading to the same conclusions: the inverse model is clearly able to predict the mechanical state (ϵ_p, σ) accurately from the knowledge of magnetic signature despite the large domain of possible solutions. The use of GA and NMA optimization algorithms allowed for a fast convergence and a low calculation cost despite the high complexity of the objective function.

7. Conclusion

In this paper, an artificial neural networks (ANNs) modeling of the effect of tensile plastic strain mixed with applied uniaxial stress on magnetic behavior of a pipeline steel has been proposed.

The ANN model was first built and then its parameters were identified thanks to learning data made up of measurements carried out on a first specimen (specimen A). About 60% of the randomly chosen data was used. The remaining 40% were used for a validation step. The model was then tested by comparing its results to experimental results obtained with a second specimen (specimen B) subjected to the same mechanical loading conditions as the first one. The model gives very satisfactory results, going well beyond the possibilities of other phenomenological or physically based models available in the literature. It should be noticed that the experimental identification data have been supplemented by a few rules relating in particular to a few physical limits,

making it possible to obtain solutions outside the experimental range and consistent with general trends. This model gives excellent results for maximal and remanent magnetization. Discrepancies with experiments are stronger for coercive field since its variations with stress, plastic strain and maximal magnetic field are strongly non-linear and non-monotonous.

Based on this result, a reverse identification procedure has been implemented. This procedure is using four magnetic input parameters, namely the maximal magnetic field strength H_{max} , maximal magnetization M_{max} , coercive field H_c and remanent magnetization M_r . Plastic deformation level ϵ_p and tensile stress σ are the output parameters. The procedure has been applied to find the mechanical state associated with four different magnetic signatures. A unique and accurate solution has been obtained for all cases.

It must however be recalled that inverse procedure is restricted to uniaxial stress and plastic strain obtained by tensile loading. Extension to plastic compression and more generally to multiaxial stress situations as met in real industrial applications is a work in progress. Extension to other materials should be addressed too.

References

- [1] R. Bozorth, *Ferromagnetism*, D. Van Nostrand, 1951.
- [2] B. Cullity, *Introduction to magnetic materials*, Addison-Wesley, 1972.
- [3] E. Hug, O. Hubert, M. Clavel, Some aspects of the magnetomechanical coupling in the strengthening of non-oriented and grain-oriented 3% sife alloys, *IEEE Transactions on Magnetics* 3 (45) (1997) 493–501.
- [4] O. Hubert, M. Clavel, I. Guillot, E. Hug, Magnetism and internal stresses: concept of magnetoplastic qnisotropy, *Journal of Physic IV* 9 (1999) 207–216.
- [5] B. Makar, J. et Tanner, The effect of plastic deformation and residual stress on the permeability and magnetostriction of steels, *Journal of Magnetism and Magnetic Materials* 222 (2000) 291–304.
- [6] O. Hubert, Influence of biaxial stresses on the magnetic behaviour of an iron-cobalt sheet - experiments and modelling, *Przedglad Elektrotechniczny* 83 (2007) 70:77.
- [7] D. Jiles, Review of magnetic methods for nondestructive evaluation, *NDT International* 21 (5) (1988) 311–319. doi:10.1016/0308-9126(88)90189-7.
- [8] G. Dobmann, *Electromagnetic nondestructive evaluation*, *Studies in Applied Electromagnetics and Mechanics* 26 (2006) 340.
- [9] F. Berg, P. Kok, H. Yang, M. Aarnts, P. Meilland, T. Kebe, M. Stolzenberg, D. Krix, W. Zhu, A. Peyton, A. Martinez-de Guereanu, I. Gutierrez,

- D. Jorge-Badiola, M. Malmström, A. Volker, A. Duijster, H. Wirdelius, A. Boström, C. Mocci, P. Lombard, Product Uniformity Control - A Research Collaboration of European Steel Industries to Non-Destructive Evaluation of Microstructure and Mechanical Properties, 2018.
- [10] B. Gupta, B. Ducharne, T. Uchimoto, G. Sebald, T. Miyazaki, T. Takagi, Non-destructive testing on creep degraded 12% cr-mo-w-v ferritic test samples using barkhausen noise, *Journal of Magnetism and Magnetic Materials* 498 (2020) 166102. doi:10.1016/j.jmmm.2019.166102.
- [11] J. Furtado, D. Gary, O. Hubert, A. Ouaddi, Method for detecting at least one fault within a ferromagnetic structure, european Patent 3862738A1 (2021).
URL <https://patents.google.com/patent/EP3862738A1/en>
- [12] Z. Maazaz, O. Hubert, E. Fnaiech, L. Kassir, Effect of plastic straining on the remanent magnetization of ferritic-pearlitic steel: Experimental and modeling aspects, *AIP Advances* 11 (2) (2021) 025015. doi:10.1063/9.0000237.
- [13] E. A. Fnaiech, S. Munschy, M. Marzin, S. Rohart, Large stand-off magnetometry (lsm) for buried pipeline inspection: Influence of dent depth on residual magnetic signal, Pipeline Technology Conference, Berlin (2020).
- [14] A. Kumar, A. Arockiarajan, Evolution of nonlinear magneto-elastic constitutive laws in ferromagnetic materials: A comprehensive review, *Journal of Magnetism and Magnetic Materials* 546 (2022) 168821. doi:10.1016/j.jmmm.2021.168821.
- [15] L. Daniel, L. Bernard, O. Hubert, Multiscale modeling of magnetic materials, in: A.-G. Olabi (Ed.), *Encyclopedia of Smart Materials*, Elsevier, Oxford, 2022, pp. 32–49.
- [16] S. Lazreg, O. Hubert, A multidomain modeling of the magnetoelastic behavior for nondestructive evaluation, *Journal of Applied Physics* 109 (2011) 07E508. doi:10.1063/1.3540416.
- [17] M. Sablik, S. Rios, F. Landgraf, T. Yonamine, M. de Campos, Modeling of sharp change in magnetic hysteresis behaviour of electrical steel at small plastic deformation, *Journal of Applied Physics* 97 (2005) 10E518. doi:10.1063/1.1856191.
- [18] O. Hubert, S. Lazreg, Two phase modeling of the influence of plastic strain on the magnetic and magnetostrictive behaviors of ferromagnetic materials, *Journal of Magnetism and Magnetic Materials* 424 (2017) 421–442.
- [19] N. Baumgartinger, C. Krell, H. PfuK tzner, G. Krismanic, Application of neural networks for the prediction of multidirectional magnetostriction, *Journal of Magnetism and Magnetic Materials* 424 (2000) 421–442.

- [20] W. Zhenwei, F. Yuan, Y. Pengxin, Q. Fasheng, T. Guiyun, W. Wai-Lok, Crack characterization in ferromagnetic steels by pulsed eddy current technique based on ga-bp neural network model, *Journal of Magnetism and Magnetic Materials* 424 (2000) 421–442.
- [21] D. Makaveev, L. Dupre, M. D. Wulf, J. Melkebeek, Dynamic hysteresis modelling using feed-forward neural networks, *Journal of Magnetism and Magnetic Materials* (2003) 256–258.
- [22] R. Liu, A. Kumar, Z. Chen, A. Agrawal, V. Sundararaghavan, A. Choudhary, A predictive machine learning approach for microstructure optimization and materials design, *Scientific reports* 5 (2015) 11551. doi:10.1038/srep11551.
- [23] O. Hubert, Multiscale magneto-elastic modeling of magnetic materials including isotropic second order stress effect, *Journal of Magnetism and Magnetic Materials* 491 (2019) 165564. doi:10.1016/j.jmmm.2019.165564.
- [24] L. Lolloz, S. Pattofatto, O. Hubert, Application of piezomagnetism for the measurement of stress during an impact, *Journal of Electrical Engineering* 57 (8) (2006) 15–20.
- [25] O. Perevertov, Influence of the applied elastic tensile and compressive stress on the hysteresis curves of fe-3%si non-oriented steel, *Journal of Magnetism and Magnetic Materials* 428 (2017) 223–228. doi:10.1016/j.jmmm.2016.12.040.
- [26] J. Degauque, B. Astie, J. Porteseil, R. Vergne, Influence of the grain size on the magnetic and magnetomechanical properties of high-purity iron, *Journal of Magnetism and Magnetic Materials* 26 (1) (1982) 261–263. doi:10.1016/0304-8853(82)90166-4.
- [27] H. Hilzinger, H. Kronmüller, Statistical theory of the pinning of bloch walls by randomly distributed defects, *Journal of Magnetism and Magnetic Materials* 2 (1) (1975) 11–17. doi:10.1016/0304-8853(75)90098-0.
- [28] H. Mughrabi, Dislocation wall and cell structures and long-range internal stresses in deformed metal crystals, *Acta Metallurgica* 31 (9) (1983) 1367–1379. doi:10.1016/0001-6160(83)90007-X.
- [29] E. Hug, O. Hubert, M. Clavel, Influence of the plastic anisotropy on the magnetic properties of a nonoriented 3% silicon iron, *Journal of Applied Physics* 79 (8) (1996) 4571–4573. doi:10.1063/1.361730.
- [30] R. Bozorth, H. Williams, Effect of small stresses on magnetic properties, *Reviews of Modern Physics* (1945) 72–80.
- [31] P. Kim, *Matlab Deep learning*, 2017.

- [32] J. F. Barbosa, J. A. Correia, R. F. Júnior, A. D. Jesus, Fatigue life prediction of metallic materials considering mean stress effects by means of an artificial neural network, *International Journal of Fatigue* (2020).
- [33] E. Alsina, M. Bortolini, M. Gamberi, A. Regattieri, Artificial neural network optimisation for monthly average daily global solar radiation prediction, *Energy Conversion and Management* 120 (2016) 320–329. doi:10.1016/j.enconman.2016.04.101.
- [34] Y. El Mghouchi, E. Chham, E. Zemmouri, A. El Bouardi, Assessment of different combinations of meteorological parameters for predicting daily global solar radiation using artificial neural networks, *Building and Environment* 149 (2019) 607–622. doi:10.1016/j.buildenv.2018.12.055.
- [35] M. R.R., D. Sathyan, Modelling the hardened properties of steel fiber reinforced concrete using ann, *Materials Today: Proceedings* (2021). doi:10.1016/j.matpr.2021.08.311.
- [36] T. Zhang, Solving large scale linear prediction problems using stochastic gradient descent algorithms, in: *Proceedings of the Twenty-First International Conference on Machine Learning, ICML '04*, Association for Computing Machinery, New York, NY, USA, 2004, p. 116. doi:10.1145/1015330.1015332.
- [37] X. Peng, L. Li, F.-Y. Wang, Accelerating minibatch stochastic gradient descent using typicality sampling., *IEEE transactions on neural networks and learning systems* 31 (11 2020). doi:10.1109/TNNLS.2019.2957003.
- [38] D. P. Kingma, J. Ba, Adam: A method for stochastic optimization (2017). arXiv:1412.6980.
- [39] J. C. Lagarias, J. A. Reeds, M. H. Wright, P. E. Wright, Convergence properties of the nelder–mead simplex method in low dimensions, *SIAM Journal on Optimization* 9 (1) (1998) 112–147. doi:10.1137/S1052623496303470.
- [40] P. Wang, T. E. Shoup, Parameter sensitivity study of the nelder–mead simplex method, *Advances in engineering software* 42 (7) (2011) 529–533.
- [41] A. Ahrari, A. A. Atai, K. Deb, Simultaneous topology, shape and size optimization of truss structures by fully stressed design based on evolution strategy, *Engineering Optimization* 47 (8) (2015) 1063–1084. doi:10.1080/0305215X.2014.947972.
- [42] O. Bozorg-Haddad, F. Hamed, H. Orouji, M. Pazoki, H. Loaiciga, A re-parameterized and improved nonlinear muskingum model for flood routing, *Water Resources Management* 29 (07 2015). doi:10.1007/s11269-015-1008-9.
- [43] J. A. Nelder, R. Mead, A Simplex Method for Function Minimization, *The Computer Journal* 7 (4) (1965) 308–313. doi:10.1093/comjnl/7.4.308.

- [44] D. Whitley, A genetic algorithm tutorial, *Statistics and Computing* 4 (2) (1994) 65–85, cited By 1632. doi:10.1007/BF00175354.
- [45] B. L. DeCost, E. A. Holm, A computer vision approach for automated analysis and classification of microstructural image data, *Computational Materials Science* 110 (2015) 126–133. doi:10.1016/j.commatsci.2015.08.011.
- [46] T.-T. Wong, P.-Y. Yeh, Reliable accuracy estimates from k-fold cross validation, *IEEE Transactions on Knowledge and Data Engineering* 32 (8) (2020) 1586–1594. doi:10.1109/TKDE.2019.2912815.

Appendix A. Experimental results carried out with sample B

Figure A.21 gathers different magnetic indicators for specimen B. Results are of course close to results obtained with specimen A (see figure 6). But some differences related to material and testing conditions variability can be observed. These results have been used for ANN model validation process.

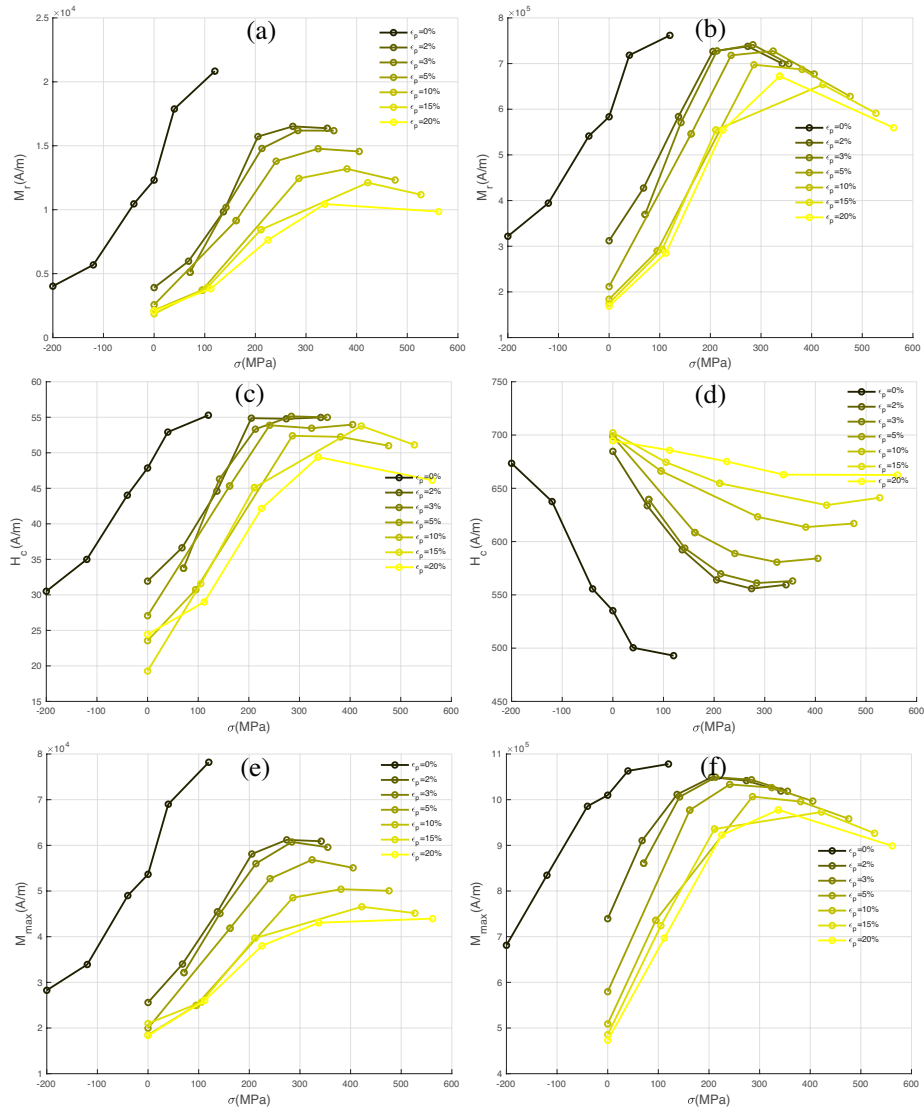


Figure A.21: Magnetic indicators for specimen B - remanent magnetization according to mechanical stress (a) $H_{max} = 230 A/m$, (b) $H_{max} = 2250 A/m$; coercive field according to mechanical stress (c) $H_{max} = 230 A/m$, (d) $H_{max} = 2250 A/m$; maximum magnetization according to mechanical stress (e) $H_{max} = 230 A/m$, (f) $H_{max} = 2250 A/m$.

Appendix B. ANN training process

The training process is carried out in two steps. The first step consists in a forward propagation that calculates the output from the input (feed).

$$\begin{cases} Y_1(n) = f(W_1(n)^T X(n)) \\ Y_{out}(n) = f(W_2(n)^T Y_1(n)) \end{cases} \quad (\text{B.1})$$

where $f()$ is the activation function, $X(n)$ is the input vector (B.2) with M elements, Y_1 is the output of the hidden layer (B.3), $Y_{out}(n)$ is the output of the system obtained by equation (B.1), $W_1(n)$ and $W_2(n)$ are weight vectors illustrated in figure B.22 and defined by equations (B.4) and (B.5).

$$X(n) = [X_1(n) X_2(n) \dots X_M(n)]^T \quad (\text{B.2})$$

$$Y_1(n) = [y_1(n) y_2(n) \dots y_K(n)]^T \quad (\text{B.3})$$

$$W_1(n) = \begin{pmatrix} w_{1,11}(n) & w_{1,12}(n) & \dots & w_{1,1M}(n) \\ w_{1,21}(n) & w_{1,22}(n) & \dots & w_{1,2M}(n) \\ \vdots & \vdots & \vdots & \vdots \\ w_{1,K1}(n) & w_{1,K2}(n) & \dots & w_{1,KM}(n) \end{pmatrix}^T \quad (\text{B.4})$$

$$W_2(n) = [w_{2,1}(n) w_{2,2}(n) \dots w_{2,K}(n)]^T \quad (\text{B.5})$$

The second step is back-propagation. It propagates the calculated error term from the output layer back to the input layer. The cost function of one training is defined as :

$$J(X(n), d(n)) = |Y_{out}(n) - d(n)|^2 \quad (\text{B.6})$$

Where $d(n)$ is the desired output. The cost function for the whole training is defined as :

$$J(X, d) = \sum_{n=1}^T J(X(n), d(n)) \quad (\text{B.7})$$

Where T is the total number of training sets.

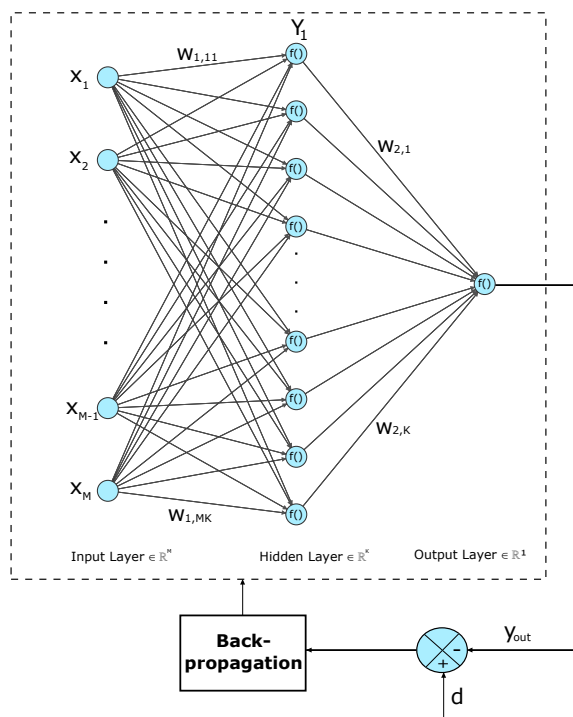


Figure B.22: Typical ANN structure with one hidden layer and one output.